

2010-01-01

Development Of Nanotube Hexaniobate For Photocatalytic Production Of Hydrogen From Water

Saroja Pradhan

University of Texas at El Paso, spradhan@miners.utep.edu

Follow this and additional works at: https://digitalcommons.utep.edu/open_etd



Part of the [Chemistry Commons](#)

Recommended Citation

Pradhan, Saroja, "Development Of Nanotube Hexaniobate For Photocatalytic Production Of Hydrogen From Water" (2010). *Open Access Theses & Dissertations*. 2563.
https://digitalcommons.utep.edu/open_etd/2563

This is brought to you for free and open access by DigitalCommons@UTEP. It has been accepted for inclusion in Open Access Theses & Dissertations by an authorized administrator of DigitalCommons@UTEP. For more information, please contact lweber@utep.edu.

DEVELOPMENT OF NANOTUBE HEXANIOWATE FOR
PHOTOCATALYTIC PRODUCTION OF
HYDROGEN FROM WATER

SAROJA PRADHAN

Department of Chemistry

APPROVED:

Geoffrey B. Saupe, Ph.D., Chair

Joanne T. Ellzey, Ph.D.

Bonnie M. Gunn, Ph.D.

Jose E. Nunez, Ph.D.

Patricia D. Witherspoon, Ph.D.
Dean of the Graduate School

Copyright ©

by

Saroja Pradhan

2010

Dedication

To my father Amber Kumar Pradhan and mother Subhadra Devi Pradhan for making me who I am today. To my brother and sisters, for their unconditional love and support. To my teachers, friends and students for having faith in me.

DEVELOPMENT OF NANOTUBE HEXANIOWATE FOR
PHOTOCATALYTIC PRODUCTION OF
HYDROGEN FROM WATER

by

SAROJA PRADHAN B.Sc.

THESIS

Presented to the Faculty of the Graduate School of
The University of Texas at El Paso
in Partial Fulfillment
of the Requirements
for the Degree of

MASTER OF SCIENCE

Department of Chemistry
THE UNIVERSITY OF TEXAS AT EL PASO
December 2010

Acknowledgements

I would first like to thank and express my deepest thanks to Dr. Geoffrey Saupe, my master's research advisor, for all his support and guidance during my two and a half years at UTEP. I would like to thank my committee members: Dr. Joanne T. Ellzey, Dr. Bonnie M. Gunn and Dr. Jose E. Nunez for their guidance, suggestions and time dedicated to review my thesis.

Special thanks to Dr. Mahsa Hosseini for her supervision, encouragement and helping me with so many areas of my research. I would also like to thank all my fellow colleagues in Dr. Saupe's Lab: Dr. Sarif Masud, Dr. Maryam Zarei Chaleshtori and Mabruka Hadidan for their friendship and support. I would also like to thank my good friends I have made here at UTEP during my studies Rudy Guerrero, Christina Gonzalez, Yong Zhao, Griselda A. Lopez, Robert Moreno, Jeffrey Hernandez, Andrew Pardo and many more. I would like to thank the following faculty members for allowing me access to their labs and instruments: Dr. Shizue Mito for allowing me to use the GC, Dr. Jorge Gardea-Torresdey and Dr. Jose Peralta for the use of the ICP-OES and XRF with the assistance of Angel Hernandez and Dr. Lijuan Zhao, Dr. Joanne T. Ellzey and her research assistant Marian Viveros for the use of the TEM, which is partially funded by the Analytical Cytology Core Facility, Border Biomedical Research Center, Dr. Carl Dirk for the use of the UV-vis. I would like to express my gratitude to Lucema Armenta, Frank Reyes, Grace Awad, Alejandro Carrillo and the entire faculty and staff of the chemistry department for all their support and help.

Lastly and most importantly, I would like to thank the Bhutanese Student Association at UTEP and my family for their love and support.

Table of Contents

Dedication	iii
Acknowledgements	v
Table of Contents	vi
List of Tables	viii
List of Figures	ix
Chapter 1: Introduction	1
1.1. Energy Background	1
1.2. Renewable Energy	5
1.3. Inorganic Photocatalysts	6
1.3.1. Semiconductor Photocatalysis	6
1.4. Importance of Semiconductor Porous Metal Oxides	8
1.5. Objectives for this Research	10
Chapter 2: Methods and Materials	12
2.1. Synthesis of Porous $\text{H}_4\text{Nb}_6\text{O}_{17}$	12
2.1.1. Solid State Synthetic Reaction and Programming of the Furnace	13
2.1.2. Acid exchange of $\text{K}_4\text{Nb}_6\text{O}_{17}$	14
2.1.3. Preparation of single lamellar sheet colloid: Exfoliation	15
2.1.4. Precipitation	16
2.1.5. Washing	18
2.1.6. Carbon dioxide drying	19
2.1.7. Topotactic dehydration	22
2.2. Characterization of the Porous Oxide Materials (POX)	23
2.2.1. Transmission Electron Microscopy (TEM)	24
2.2.2. Scanning Electron Microscopy (SEM)	26
2.2.3. X- ray Diffraction (XRD)	27
2.2.4. X-ray fluorescence spectroscopy (XRF)	28
2.2.5. Accelerated Surface Area and Porosimetry System	29
2.2.6. Inductively Coupled Plasma – Optical Emission Spectroscopy (ICP-OES)	33
2.2.7. UV – visible Scanning Spectrophotometer	35

2.3. Results And Discussions.....	37
2.3.1. TEM Images.....	37
2.3.2. SEM Images.....	41
2.3.3. XRD Patterns of the Porous Metal Oxides	44
2.3.4. X-Ray Fluorescence Spectrometry (XRF).....	46
2.3.5. BET Surface Area and Pore Analysis of Porous Metal Oxides.....	48
2.3.6. ICP-OES analysis.....	50
2.3.7. UV – visible Reflectance Spectrometry.....	50
Chapter 3: Hydrogen Production under Ultraviolet Light	53
3.1. Introduction.....	53
3.1.1. Experimental set up for metal deposition	53
3.1.2. SEM analysis of the metal deposited POX materials	55
3.1.3. TEM analysis of metal deposited POX materials	59
3.1.4. Inductively Coupled Plasma – Optical Emission Spectroscopy Analysis	62
3.2. Calibration curve for hydrogen measurement.....	62
3.3. Hydrogen Evolution by Non-Topo and Topo POX Materials.....	63
3.3.1. Experimental set up.....	63
3.3.2. Hydrogen Evolution by Non Topo $H_4Nb_6O_{17}$	64
3.3.3. Comparison of Hydrogen Evolution of Non Topo and Topo POX.....	67
3.4. Quantum Efficiency of Hydrogen Evolution.....	68
3.5. Conclusions.....	70
References.....	71
Curriculum Vita	76

List of Tables

Table 2.1: BET surface area measurement for non-topo and topo POX	48
Table 2.2: ICP-OES analysis of topotactic dehydrated hexaniobate porous metal oxides.....	50
Table 2.3: Onset of absorbance and energy band gap for hexaniobate metal oxide.....	51
Table 3.1: Different amounts of reagents for different percentages of metal loading onto the POX.....	54
Table 3.2: ICP-OES analysis for the metal deposited solid POX and its supernatant.....	62
Table 3.3: Summary of Apparent Quantum Yields for different percentages metal loading.....	70

List of Figures

Figure 1.1: The energy transition over time.....	2
Figure 1.2: Four main energy end-use sectors.....	2
Figure 1.3: World energy consumption, 1970 – 2025.	3
Figure 1.4: Global energy consumption by fuel type (2005).....	4
Figure 1.7: Various applications of porous metal oxides.	9
Figure 1.8: Number of publications on porous metal oxides listed in Scifinder Scholar.	10
Figure 2.1: Block diagram showing the synthesis of porous metal oxide, $\text{H}_4\text{Nb}_6\text{O}_{17}$	12
Figure 2.2: Schematic of furnace temperature program for synthesizing $\text{K}_4\text{Nb}_6\text{O}_{17}$	13
Figure 2.3: $\text{K}_4\text{Nb}_6\text{O}_{17}$ has a layered structures with exchangeable cations.....	15
Figure 2.4: Acid base neutralization reactions between $\text{H}_4\text{Nb}_6\text{O}_{17}$ and TBAOH.....	16
Figure 2.5: Exfoliated colloidal sheets.....	16
Figure 2.6: Glass vial with both sides closed by vial caps. The porous material is visible inside the vial.....	17
Figure 2.7: Schematic representation of the formation of nanotubes.	18
Figure 2.8: Washing of the metal oxide aggregates.....	19
Figure 2.9: Phase diagram of Carbon dioxide.	20
Figure 2.11: Dried porous metal oxides (non topo POX).....	22
Figure 2.12: Porous metal oxide material heated to form topotactic dehydrated porous metal oxide.....	23
Figure 2.13: Transmission Electron Microscope.	25
Figure 2.14: Scanning Electron Microscope.....	26
Figure 2.15: Production of secondary X-rays in XRF.	29

Figure 2.16: The ASAP 2020 (Micromeritics) surface area analyzer (BET).	30
Figure 2.17: Parameters for degassing the porous metal oxides in ASAP 2020 porosity system..	32
Figure 2.18: Parameters for analyzing the porous aggregates samples in ASAP 2020 porosity. 33	
Figure 2.19: ICP-OES, Torch for Trace element detection.	34
Figure 2.20: Working of the UV-Vis Spectrophotometer.	36
Figure 2.21 a-b: TEM images of colloid material.....	38
Figure 2.22 a-b: TEM images of non-topo POX ($\text{H}_4\text{Nb}_6\text{O}_{17}$).....	39
Figure 2.23a-b: TEM images of topotactic dehydrated POX (Nb_6O_{15}).....	40
Figure 2.24a, b and c: SEM images of non-topo POX material ($\text{H}_4\text{Nb}_6\text{O}_{17}$).....	42
Figure 2.25a, b and c: SEM images of topotactic dehydrated POX material (Nb_6O_{15}).....	43
Figure 2.26: XRD patterns of parent material $\text{K}_4\text{Nb}_6\text{O}_{17}$, acid exchanged $\text{H}_4\text{Nb}_6\text{O}_{17}$, non-topo ($\text{H}_4\text{Nb}_6\text{O}_{17}$) and topo (Nb_6O_{15}).....	45
Figure 2.27a: Typical X-ray fluorescence data for POX (non-topo) samples.	46
Figure 2.27b: Typical X-ray fluorescence image for POX (topo) samples	47
Figure 2.28: BJH Desorption dV/dD Pore Volume of non-topo POX.	49
Figure 2.29: BJH Desorption dV/dD Pore Volume of topo POX.	49
Figure 2.30: Determination of onset of absorbance.....	51
Figure 2.31: Absorbance data for the hexaniobate samples (parent materials, acid..... exchanged, non topo and topo POX).	52
Figure 3.1: Quartz tube with a POX suspension inside showing reduction of metallic platinum on the material surface. After deposition,the color of the POX changed from white to grey.....	55
Figure 3.2(a-b): SEM images of platinum deposited on non-topo POX material.	57

Figure 3.3 (a-b): SEM images of platinum deposited on topo POX material.....	58
Figure 3.5 (a-b): TEM images of platinum deposited on topo POX material.	61
Figure 3.6: Hydrogen Calibration graph.....	63
Figure 3.7: Experimental set up for hydrogen evolution under UV light.....	64
Figure 3.8: Hydrogen evolution by non topo $\text{H}_4\text{Nb}_6\text{O}_{17}$ at different loading percentage of platinum.	65
Figure 3.9: 2% platinum loaded non topo POX.....	66
Figure 3.10: 0.5% platinum loaded non topo POX.....	67
Figure 3.11: Hydrogen evolution by 5% metal loaded non topo and topo POX.....	68

Chapter 1: Introduction

1.1. Energy Background

Energy is the foundation of modern economies, both at a national and international level. The global energy consumption is increasing at a ever faster rate, due to overall improvements in human lifestyles. The global energy demand is expected to rise by 35 percent by 2030.¹ Energy consumption is high in most developed countries, while, developing countries need to consume more energy to ensure economic growth.

Energy sources and technology change over time and each is influenced by the other. In the United States during the 1850s wood was the biggest source of energy. By the 1900s coal use predominated over wood. By the 1950s, oil overtook coal as more people owned cars and rail transport shifted from coal to petrol. From 1950 onwards, one also saw the introduction and growth of hydroelectric power, nuclear energy and natural gas (Figure 1.1).¹ In the future, it is likely that shifts in energy usage and technology will continue. Over the past 150 years, the growth of modern energy and technology has had a positive impact on the enhancement of human lifestyles. Gaining access to energy represents hope and opportunity, which means superior transportation, increased commerce, expanded industry and greater access to health care and other social services. It is estimated that the economic growth will be led by countries not in the Organization for Economic and Co-operation and Development (OECD), such as India and China, where energy usage will rise by about 65 percent by 2030.¹

When broken down, there are four main energy end-use sectors, viz.: transportation, industrial, residential/commercial and electric power generation (Figure 1.2).

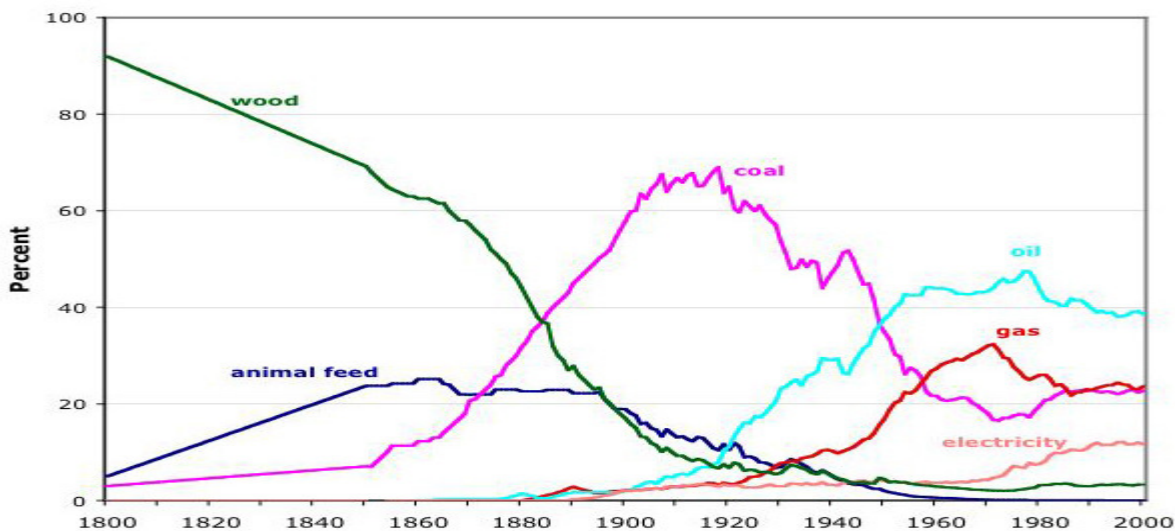


Figure 1.1: The energy transition over time.²

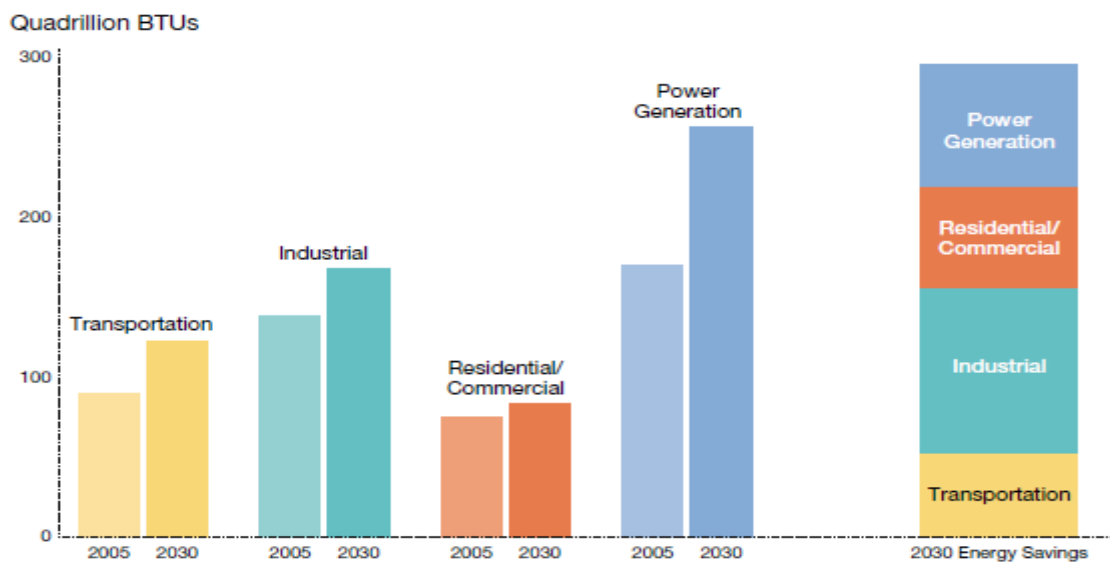


Figure 1.2: Four main energy end-use sectors.¹

As seen in Figure 1.2, power generation is not only the largest energy demanding sector, but also the fastest growing of all the sectors. It is estimated that by 2030, this sector will represent 55 percent of the total growth in energy demand.¹ Power generation is followed by

transportation demand, which will grow 40 percent by 2030. The industrial and residential/commercial sectors will grow at a relatively slow pace as seen in Figure 1.2. In total, the global energy demand is expected to grow an average of 1.2 percent per year between 2005 and 2030.¹

The total energy consumption in 2008 was 15 terawatts, with about 85 percent derived from the consumption of fossil fuels.³ Figure 1.3 shows the increasing trend in the usage of the fossil fuels. Though the use of renewable fuels is on the rise, the use of fossil fuels is dominant. Out of the total energy sources in use today, about 37% comes from oil, 26% from coal, 23% from gas, 7% from nuclear power and 5% from renewable fuel (Figure 1.4).⁴

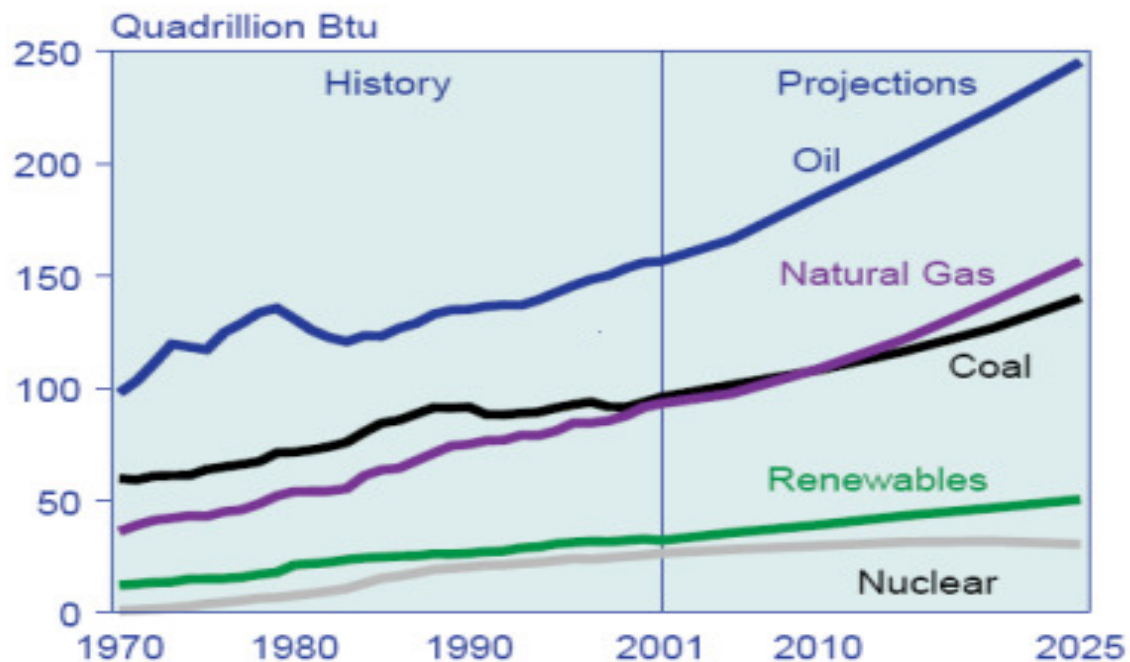


Figure 1.3: World energy consumption, 1970 – 2025.⁵

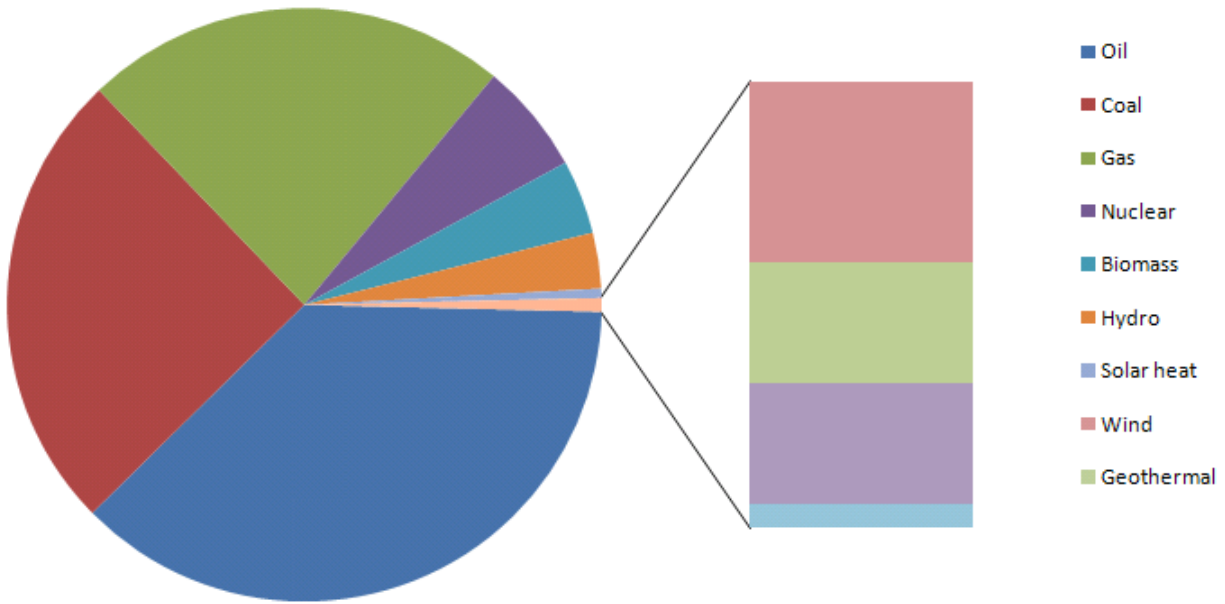


Figure 1.4: Global energy consumption by fuel type (2005).⁴

The use of fossil fuels has its own shortcomings. The majority of the world now relies on the use of fossil fuels for its energy because of its high abundance and low cost of extraction. These fossil fuels are non renewable and over time will cease to exist. This will cause the world to face an energy crisis.

Furthermore, the production and use of fossil fuels raises environmental concerns. The burning of fossil fuels produces about 21.3 billion tons of carbon dioxide per year.⁵ The increase in carbon dioxide in the earth's atmosphere acts to increase the "blanket" keeping in outgoing radiation, thereby causing global warming. The impact of global warming on the environment and living things is very extensive. High temperature raises the sea level by expanding the ocean water, melting the mountain glaciers and ice caps. The International Panel on Climate Change (IPCC) estimated that the average global sea level will rise between 0.6 to 2 feet in the next century.⁶

The burning of fossil fuels produces smog which is derived from vehicular emission and industrial exhausts to form secondary pollutants. The conversion of these fossil fuels into usable energy results in accumulation of solid waste. The waste produced, requires land space for containment and treatment as well as financial support and monitoring for wastes, which are not easily disposable. This type of waste increases the risk of toxic run off, that can poison surface and ground water sources, endangering the nearby vegetation, wildlife and marine life. The distribution of fossil fuels also poses a threat due to the possibility of spills. Seepage from foundations like oil rigs and pipelines can result in the similar destruction of habitats and wildlife.

The burning of fossil fuels also contributes to global warming which can lead to extreme weather events, an expansion of tropical diseases, and changes in timing of patterns in ecosystems.⁷ Hence, looking at the adverse effects of fossil fuels on humans, the environment, and flora and fauna, there exists an immediate need to develop low cost, high efficiency, renewable and clean energy.

1.2. Renewable Energy

Renewable energy is referred to as an energy resource that is naturally regenerated over a short time scale and derived directly or indirectly from the sun or from other natural sources.⁸ In its various forms, renewable energy is derived directly from the sun, or from heat generated deep within the earth. The global demand for energy is just 15 terawatts, while there are 89,000 terawatts of solar energy and 370 terawatts of wind energy available on the earth's surface.

There are various technologies developed to take advantage of solar energy. These applications for example are;

- Architecture and urban planning

- Agriculture and horticulture
- Solar lighting
- Water Treatment
- Solar vehicles
- Photovoltaics
- Photocatalysts

Photovoltaics (solar cells) for example convert solar energy to electrical energy. In the case of photovoltaic systems, they have to be coupled with batteries or a water electrolyzer system in order to store solar energy. Photocatalysis has an advantage over photovoltaics, as being a less expensive alternative. However, the photo conversion efficiencies of inorganic photocatalysts to convert solar energy directly into energy rich chemicals, such as hydrogen via water photolysis at present is too low for practical systems.^{9,17} Thus, there is a great need to investigate and improve inorganic photocatalytic systems in the near future.

1.3. Inorganic Photocatalysts

1.3.1. Semiconductor Photocatalysis

Photocatalysis refers to the acceleration of a photoreaction by the presence of a catalyst. There are two types of catalysts, depending on whether or not they exist in the same phase as a substrate. They are homogenous catalysts and heterogeneous catalysts. Homogenous catalysts act in the same phase as the substrate, whereas heterogeneous catalysts function in a different phase than the substrate. Heterogeneous photocatalysis involves photoreaction, occurring at the surface of the catalyst and in most cases refers to the semiconductor photocatalysis or semiconductor-sensitized photoreactions. Typically photosensitization is a chemical alteration of

a wide band gap semiconductor using a surface adsorbed dye that adsorbs light in the visible spectrum that occurs in one chemical species as a result of the initial absorption of radiation by another chemical species called photosensitizer.

In Equation 1 from Figure 1.5, the activation of the semiconductor photocatalyst is achieved through the absorption of a photon of ultra-bandgap energy. A semiconductor material consists of many electron energy levels. The band of electron energy levels filled with electrons are called the valence band (VB), while at a higher energy level, a largely vacant electron energy band called the conduction band (CB) is located. The energy difference between the two bands is called the bandgap, E_{bg} .¹⁰ The result is the promotion of an electron (e^-) from the valence band to the conduction band.

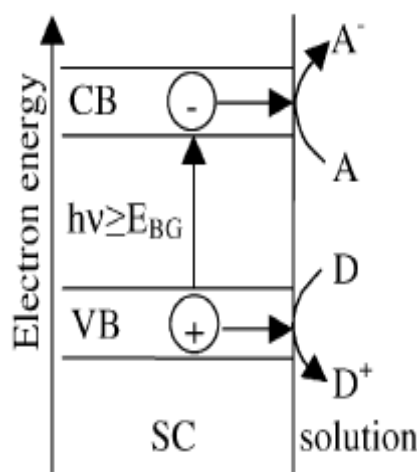
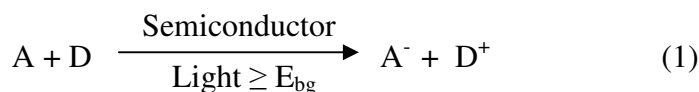


Figure 1.5: Production of conduction band electron and valence band hole in a semiconductor after absorption of a photon.¹⁰

The overall photoactivity of the semiconductor depends on the photogenerated electron-hole pair (e^- and h^+). Typically, the electron-hole pairs recombine, either at the point of origin or at the surface of the semiconducting material, generating heat in the process (Figure 1.6 a and b). If this happens, then the semiconductor will not show any photoactivity. However, if the generated electron and hole make it to the surface of the semiconducting material, they will interact with the surface species available. If an electron donor (D) happens to be present at the surface of the semiconductor, then the hole can react with it to produce an oxidized product, D^+ (Figure 1.6 d). Similarly, if an electron acceptor, A, is present at the surface, then the electron can react with it to generate a reduced product, A^- (Figure 1.6 c).¹⁰

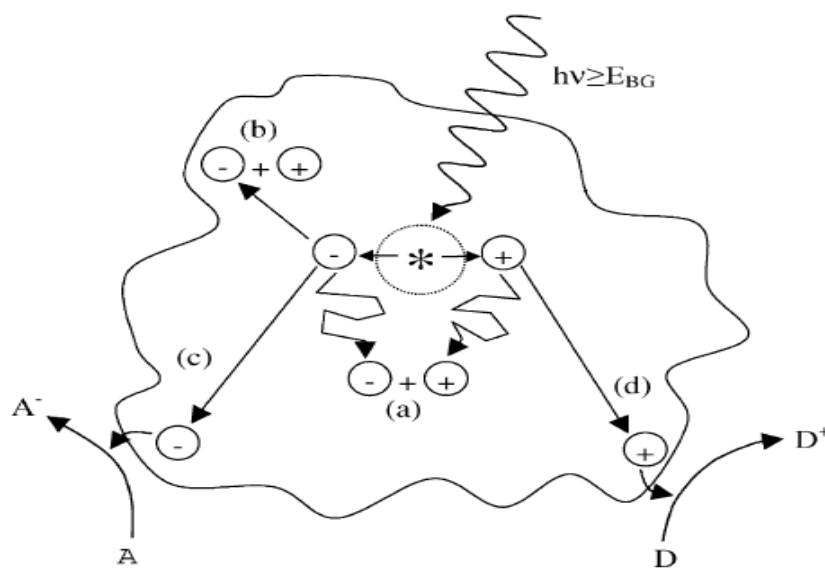


Figure 1.6: Processes occurring after absorption of a photon in a semiconducting material.¹⁰

1.4. Importance of Semiconductor Porous Metal Oxides

Porous metal oxide solids have been and continue to be excellent topics of study. They have a wide range of functions and purposes including photocatalysts,¹¹⁻¹⁸ as molecular sieves for

adsorption separation,¹⁹⁻²¹ as immobilizing media,²² as a basis for sensors,²³⁻²⁵ to detect chemical or gases in the environment, and as an ion exchanger²⁶ (Figure 1.7).

Because of their vast application, researchers have shown great interest in the studies of porous metal oxides. Figure 1.8 shows the number of publications listed on porous material research using American Chemical Society's Scifinder Scholar database.

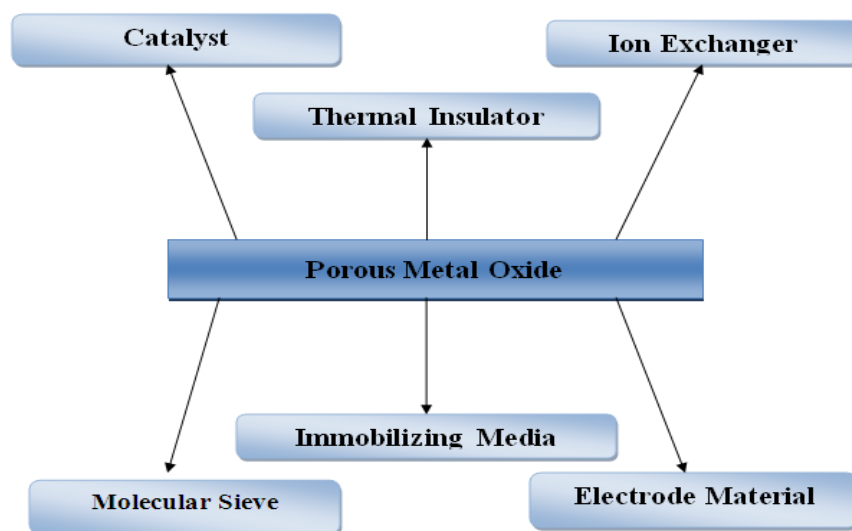


Figure 1.7: Various applications of porous metal oxides.²⁷

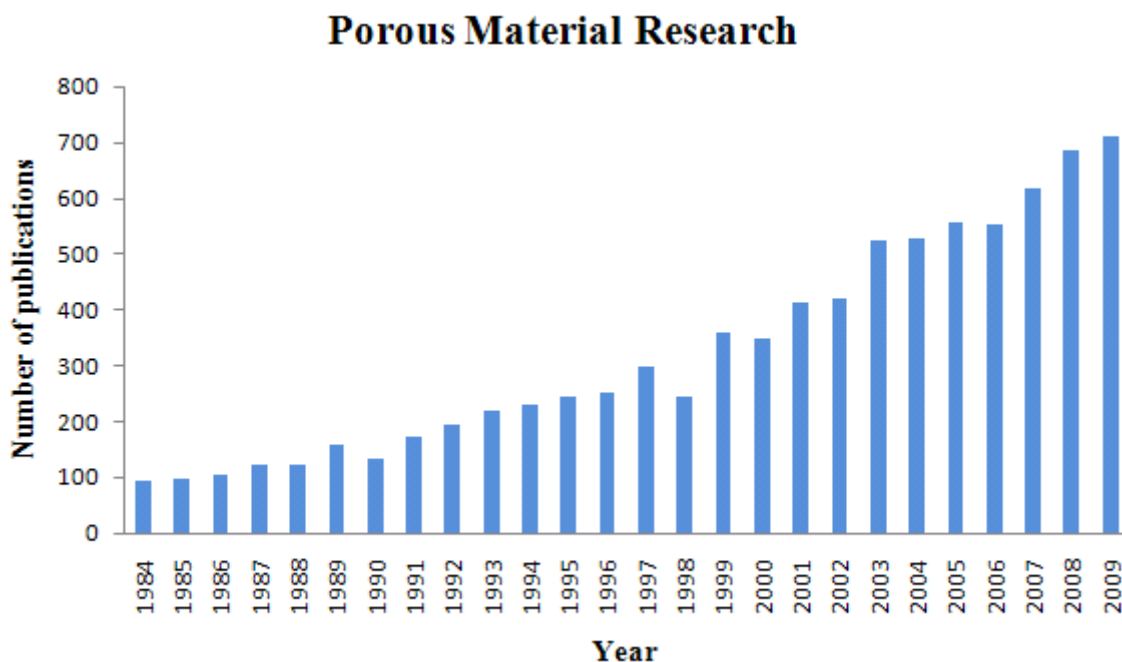


Figure 1.8: Number of publications on porous metal oxides listed in Scifinder Scholar.

1.5. Objectives for this Research

1. To explore the synthetic pathways that can lead to optimized large pore, high surface area and wide bandgap nanotubes and to characterize the synthesized porous metal oxides using the following techniques;
 - a. Transmission electron microscopy (TEM)
 - b. Scanning electron microscopy (SEM)
 - c. X-ray diffraction (XRD)
 - d. UV-Vis reflectance spectrophotometry
 - e. BET surface area analysis.
 - f. X-ray fluorescence (XRF)
 - g. Inductively coupled plasma/optical emission spectrometry (ICP-OES).

2. To develop and test new photocatalytic material for hydrogen production under ultraviolet light.
3. To determine the catalytic activity of the untreated and the thermally treated porous metal oxide products.

Chapter 2: Methods and Materials

Porous Hexaniobate, $\text{H}_4\text{Nb}_6\text{O}_{17}$, is a metal oxide derived from potassium hexaniobate ($\text{K}_4\text{Nb}_6\text{O}_{17}$) using the following synthetic steps:

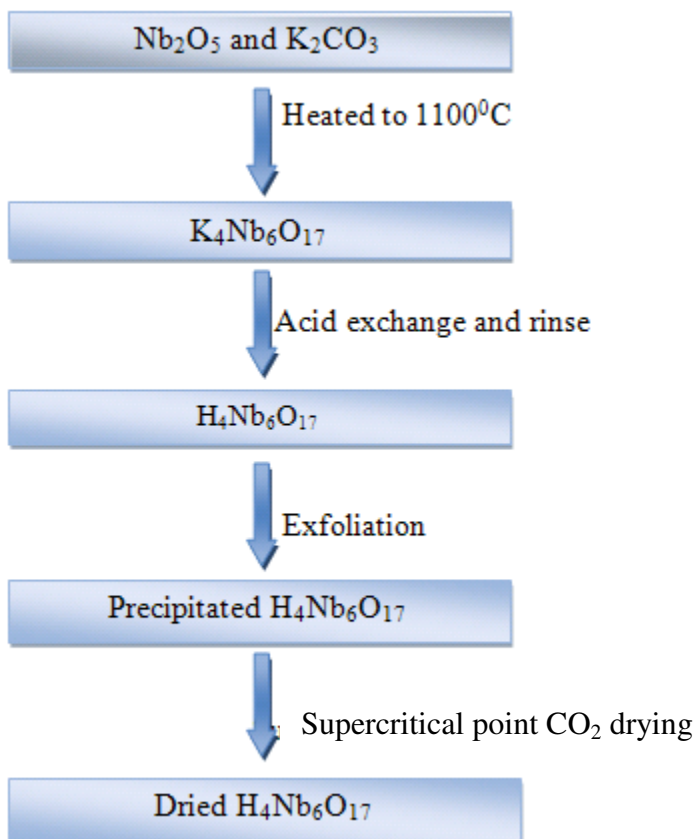
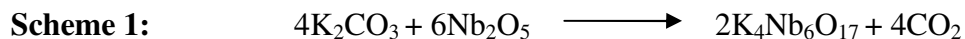


Figure 2.1: Block diagram showing the synthesis of porous metal oxide, $\text{H}_4\text{Nb}_6\text{O}_{17}$.

2.1. Synthesis of Porous $\text{H}_4\text{Nb}_6\text{O}_{17}$

Reagent grade potassium carbonate sesquihydrate, $\text{K}_2\text{CO}_3 \cdot 6\text{H}_2\text{O}$ (Fisher Chemicals, Fairlawn, New Jersey) and niobium (v) oxide (Alfa Aesar, Ward Hill, Massachusetts) were

purchased. Stoichiometric amounts of each reagent were used to produce potassium hexaniobate in a solid state reaction. A 10% excess of potassium carbonate was added to compensate for the loss of potassium as an oxide during the heating.



7.63 g of potassium carbonate was finely ground in a mortar and pestle and heated in an oven to 230 °C for two hours to drive off water. It was then mixed with 20 g of Niobium oxide and ground into a fine powder. This finely ground mixture was transferred to an alumina crucible and heated in the furnace to 1100 °C.

2.1.1. Solid State Synthetic Reaction and Programming of the Furnace

The mixture in the crucible was placed in a high temperature furnace (BF51800 series, Lindberg/Blue, NC, USA) and heated for 20 hours. Figure 2.2 below shows the temperature control over time.

For the reaction in the scheme 1, the temperature was raised to 120 °C at a rate of 10 °C per minute and was held there for the next 30 minutes. The temperature was then raised to 1100 °C at a rate of 10 °C per minute and held there for the next 20 hours, and was then allowed to cool to 25 °C. The material $\text{K}_4\text{Nb}_6\text{O}_{17}$ was then stored at ambient conditions until needed.

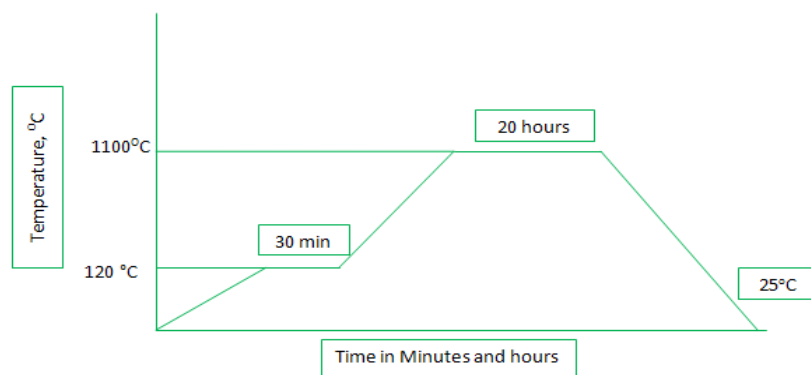


Figure 2.2: Schematic of furnace temperature program for synthesizing $\text{K}_4\text{Nb}_6\text{O}_{17}$.

2.1.2. Acid exchange of $K_4Nb_6O_{17}$

$K_4Nb_6O_{17}$ has a layered structure with potassium cations in between the layers of the metal oxide. These layered materials were converted into protonated lamellar compounds ($H_4Nb_6O_{17}$) by cationic exchange using strong acidic solutions.

Five grams of layered $K_4Nb_6O_{17}$ were measured and placed in a 500.00 mL beaker. 250.00 mL of deionized water (DI) water and 100 mL of concentrated hydrochloric acid (12 M) were added. The beaker was then covered with a parafilm and stirred for one day at 40 °C. The slurry was centrifuged at 3000 rpm for 10 minutes and the supernatant was decanted. The solid exchanged material in the bottom of the centrifuge tubes was recovered with DI water and the suspension was placed back into the beaker.

This procedure was repeated every 24 hours for four days for a total of five acid exchanges. The final suspension was again centrifuged and decanted. The residue was recovered with ethanol and the suspension was then transferred to a Petri dish. It was allowed to dry at room temperature.

The niobate has two type of interlayer regions designated as interlayer I and interlayer II. The proton exchange in layered niobate occurs easily in interlayer I, while interlayer II is difficult for proton exchange. So, the overall acid exchange process produces a material with a formula of $H_{4-x}K_xNb_6O_{17}$, where x is close to zero (Figure 2.3).²⁸

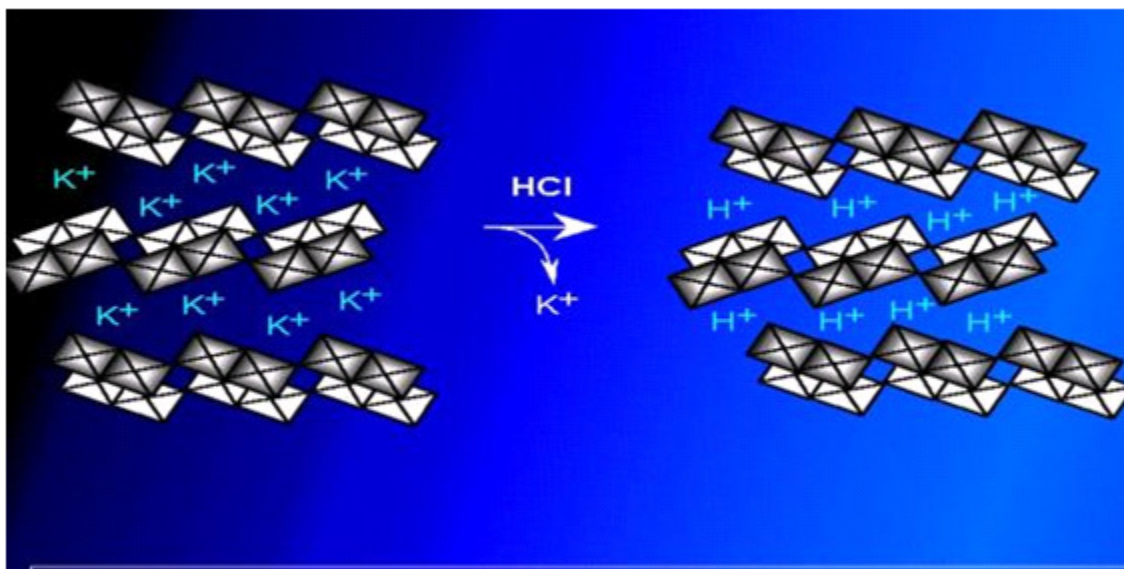


Figure 2.3: $\text{K}_4\text{Nb}_6\text{O}_{17}$ has a layered structures with exchangeable cations.

2.1.3. Preparation of single lamellar sheet colloid: Exfoliation

The transformation of lamellar oxides into single sheet colloid occurs when an aqueous suspension of $\text{H}_4\text{Nb}_6\text{O}_{17}$ reacts with Tetrabutyl ammonium hydroxide (TBAOH) by an acid base neutralization reaction.²⁹⁻³³ This neutralization reaction allows the TBA cations into the layers replacing the protons (Figure 2.4). The TBA^+ cations intercalate the interlayer spaces, resulting in the exfoliation of the individual metal oxide sheets. The exfoliated metal oxide sheets ($\text{Nb}_6\text{O}_{17}^{4-}$) are negatively charged, so they allow TBA^+ counter cations on their surface, thereby increasing the distance between the sheets.

250.00 mL of DI water was added to 2 g of acid exchanged solid and the mixture was stirred for two hours, followed by the addition of 2 drops of phenolphthalein and 1.2 mL of TBAOH. The mixture was stirred for one day. This produced the colloid of single sheets (Figure 2.5).

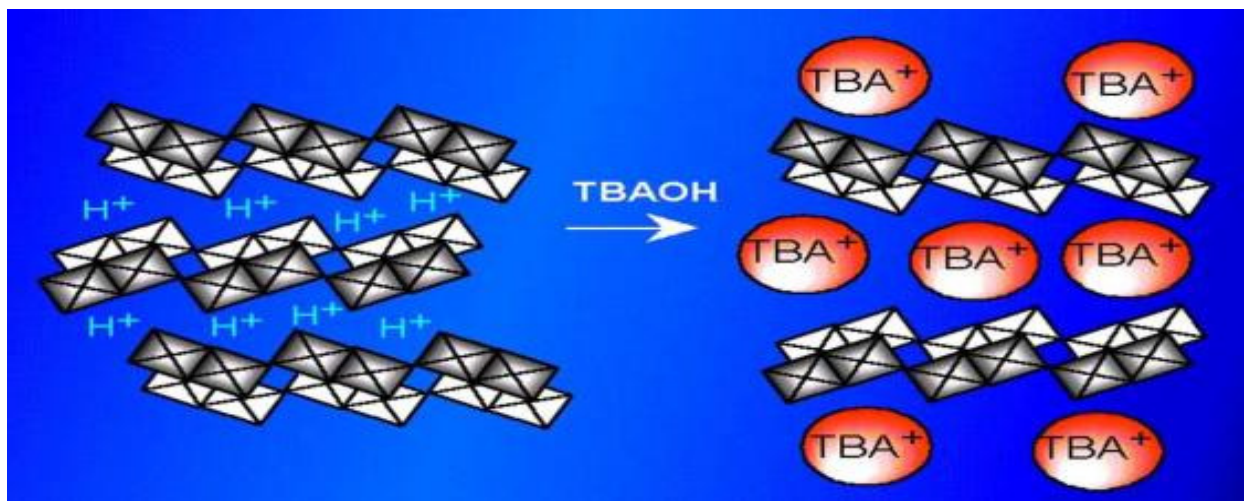


Figure 2.4: Acid base neutralization reactions between $\text{H}_4\text{Nb}_6\text{O}_{17}$ and TBAOH.

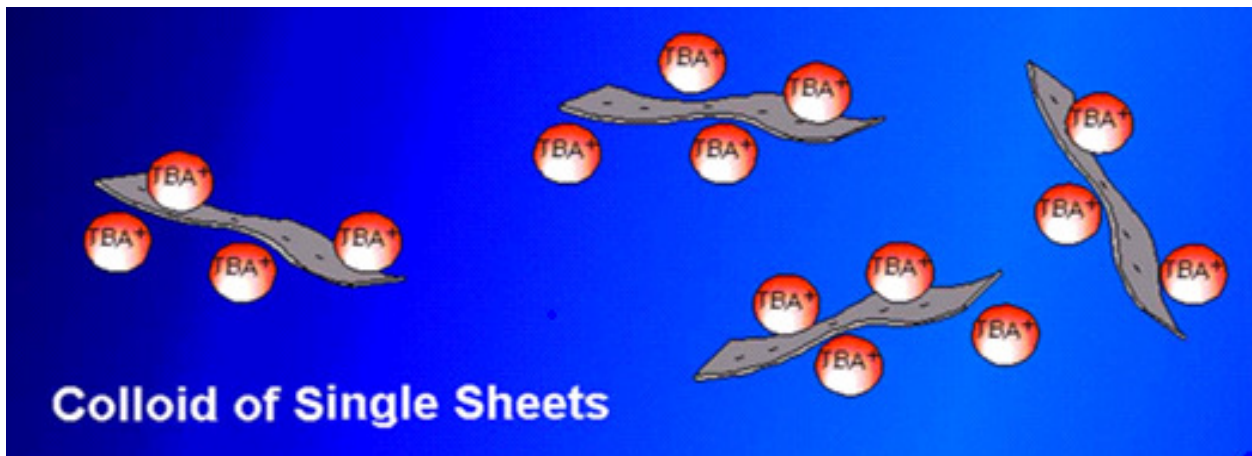


Figure 2.5: Exfoliated colloidal sheets.

2.1.4. Precipitation

8.00 mL of colloids were mixed with 16.00 mL of DI water in a borosilicate glass vial. The glass vial has both sides open with the bottom side closed with a vial cap (Figure 2.6). The mixture was thoroughly stirred and three drops of 3 M hydrochloric acid were added uniformly to this mixture down each side of the vial. The vial was then closed with a cap and the sample

was allowed to sit undisturbed for two days. During this period, the nano sheets formed aggregates, resulting in a porous solid.

In this way nanosheet colloids were precipitated with concentrated hydrochloric acid to form agglomerates stable, ultra-porous, transition metal oxide tubules. There are some hypotheses which explain the reason for the formation of nanotubes. A single oxide layer of $\text{K}_4\text{Nb}_6\text{O}_{17}$ niobate does not have inversion symmetry and the surface atom densities between two sides of the layer are different which creates a strain force that causes the sheet to roll in (Figure 2.7).³⁴⁻³⁵

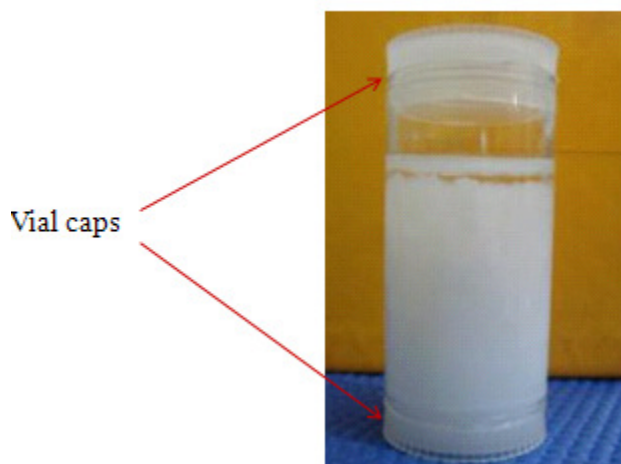


Figure 2.6: Glass vial with both sides closed by vial caps. The porous material is visible inside the vial.

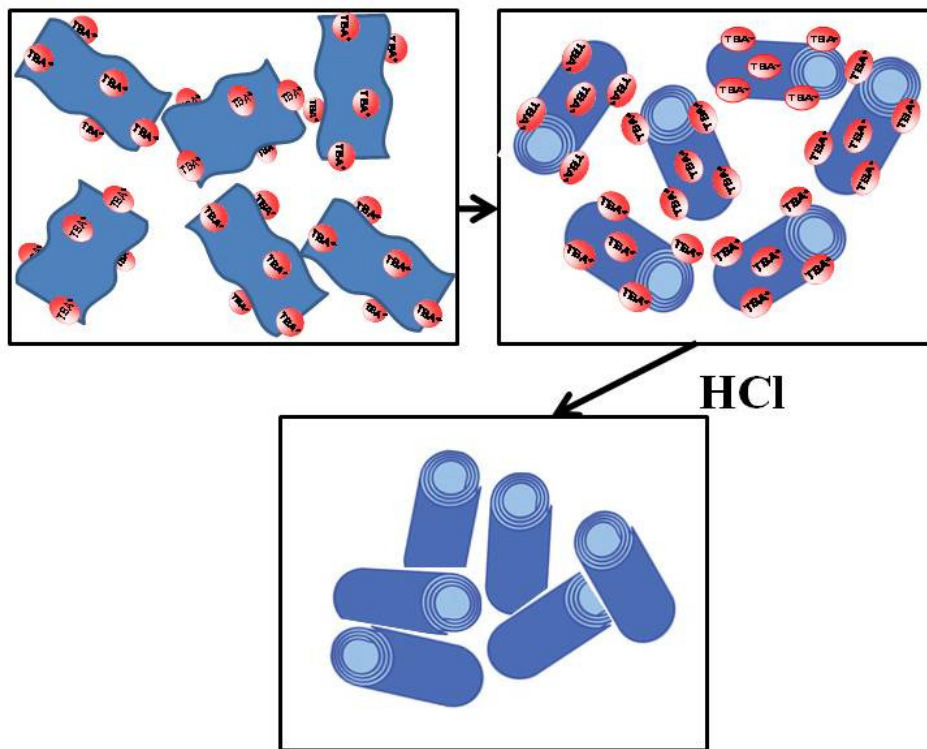


Figure 2.7: Schematic representation of the formation of nanotubes.

2.1.5. Washing

After precipitating the colloidal nanotubes into porous aggregates, it was then rinsed in a special apparatus with water, followed by ethanol and then acetone. The vial was placed on a clamp and stand, with the top of the vial connected to a 60.00 mL plastic syringe through flexible polyethylene tubing and a needle. Small holes were made in the bottom cap of the vial to allow the solvent out (Figure 2.8). 300.00 mL of water was run through the porous aggregates followed by 300.00 mL of ethanol and then 500.00 mL of acetone. After washing the nanotube aggregates with acetone, the top cap was replaced with a new one. The vial was then carefully inverted and immersed fully into a beaker of acetone and the top cap was replaced by a wire mesh cap to allow the passage of solvent during CO₂ drying steps in the critical point drying.

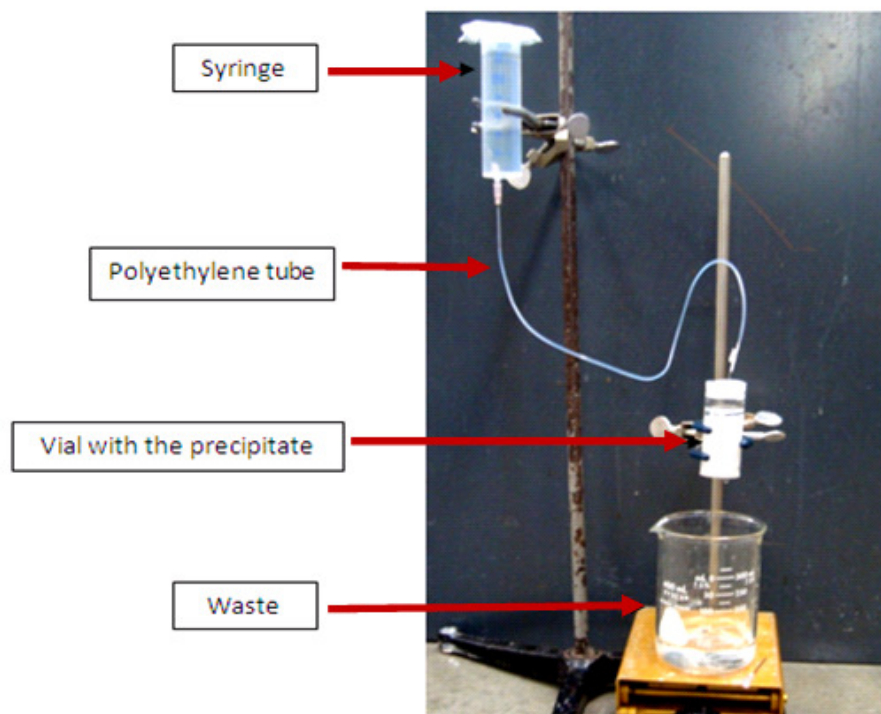


Figure 2.8: Washing of the metal oxide aggregates.

2.1.6. Carbon dioxide drying

Carbon dioxide is a gas at STP (Standard Temperature and Pressure) or exists as a solid (called “dry ice”) when frozen at $-78.5\text{ }^{\circ}\text{C}$. Carbon dioxide may exist as a liquid at room temperature if it is pressurized above 800 psi. When liquid carbon dioxide in a closed container is heated, the pressure rises and the CO_2 changes phase. Above $31\text{ }^{\circ}\text{C}$ and 72.9 atm is the critical point of CO_2 , where it adopts properties midway between a gas and a liquid (Figure 2.9). CO_2 behaves as a supercritical fluid above its critical temperature and pressure of $31.1\text{ }^{\circ}\text{C}$ and 72.9 atm respectively. At or above the critical temperature and pressure, carbon dioxide expands and fills its container just like a gas but within a density like that of a liquid. The supercritical point CO_2 drying process allows the sample to be dried without any surface tension, thereby reducing the likelihood of capillary force or solvent surface tension. The low temperature of the process

and the stability of CO₂ also allow most compounds to be extracted with little damage or denaturing.

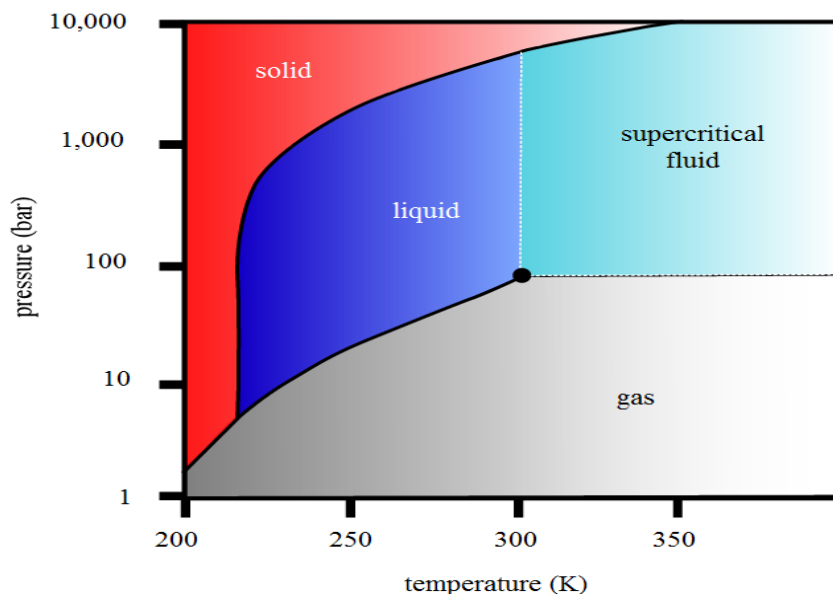


Figure 2.9: Phase diagram of carbon dioxide.³⁶

Procedure:

Supercritical point drying of the metal oxide by CO₂ was done using a drying system (Quarum Technologies, East Sussex, U.K) (Figure 2.10). The drying chamber was cleaned thoroughly and cooled by circulating cold water to 16 °C. The chamber was then half filled with acetone. The sample vial was placed inside the chamber and the chamber door was closed. The CO₂ tank valve was opened two full turns and the chamber inlet valve was also opened carefully to begin letting in the liquid CO₂ into the chamber. While the CO₂ inlet valve was open, the acetone inside the chamber was flushed out by releasing the solvent out from the bottom outlet. After a short while, there was an acetone-CO₂ phase line, which moves down as pure CO₂ comes in. The chamber was filled and emptied three times with occasional agitation to promote mixing.

Finally, the chamber was filled to $\frac{3}{4}$ capacity and all the valves were closed and also the cold water pump was turned off. The chamber temperature was then raised to 30 °C by using circulating hot water. It was then noticed that the fluid inside the chamber has expanded slightly. At this point the hot water circulation was stopped and the chamber remained the same for 20 minutes. The chamber was cooled again to 16 °C by circulating cold water and the CO₂ inlet valve was opened to let in fresh CO₂ and the outlet valve was also opened to flush out CO₂. This flushing was carried out for the next 10 minutes and finally the chamber was filled $\frac{2}{3}$ full. All the valves were closed and the chamber was heated to 40 °C by circulating hot water. During this second heating step, at around 34-35 °C, the CO₂ reached the supercritical point phase. The chamber was kept at 40 °C, for 15 minutes. The top vent was opened and very slowly released the gas at a rate of 20 psi/min. The chamber was opened, when the pressure reached the atmospheric level. The vial was taken out from the chamber and placed in a dessicator (Figure 2.11).



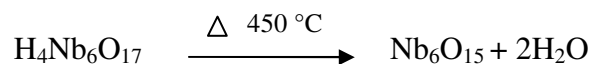
Figure 2.10: Supercritical point CO₂ chamber.



Figure 2.11: Dried porous metal oxides (non topo POX).

2.1.7. Topotactic dehydration

Dried porous metal oxide materials have ionic bonding between the layers of the metal oxide and the protons (H^+). The electronic conduction between layers would be better, if the layers were connected covalently. The porous metal oxide materials were heated at 450 °C for 2 hours in the furnace, which produced topotactic dehydrated porous metal oxides (Figure 2.12).



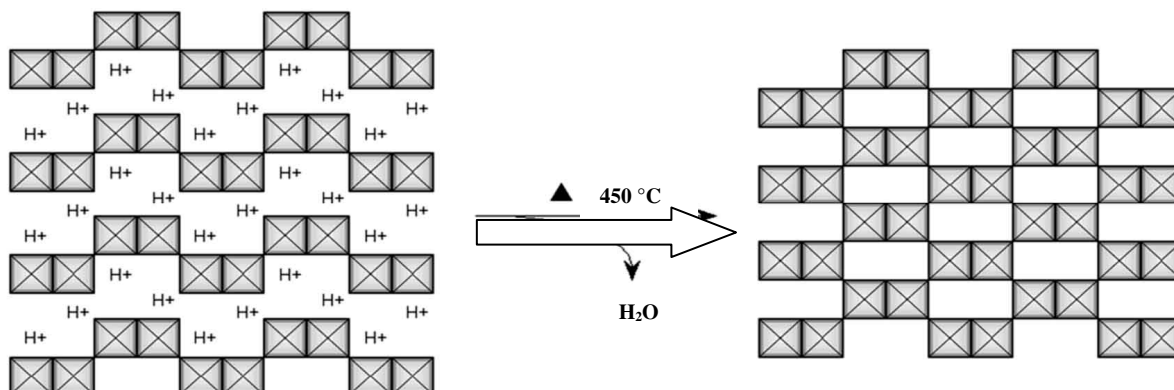


Figure 2.12: Porous metal oxide material heated to form topotactic dehydrated porous metal oxide.

Note: From here onwards, the unheated POX will be called **non-topo POX** and the topotactic dehydrated POX will be called **topo POX**.

2.2. Characterization of the Porous Oxide Materials (POX)

The porous materials synthesized were characterized for their surface morphologies, structural characteristics, surface area, pore volume, band gap and elemental analysis using technologies available in the university. The characterizations were done for the parent material ($\text{K}_4\text{Nb}_6\text{O}_{17}$), acid exchanged material ($\text{H}_4\text{Nb}_6\text{O}_{17}$), porous metal oxide material ($\text{H}_4\text{Nb}_6\text{O}_{17}$) and topotactic dehydrated porous metal oxide material (Nb_6O_{15})

Structural characterization was done with powder X-ray diffraction studies (XRD) using an XRD system (D8 Discover, Bruker Axs Inc., WI, USA). The XRD studies were done for the parent material ($\text{K}_4\text{Nb}_6\text{O}_{17}$), acid exchanged material ($\text{H}_4\text{Nb}_6\text{O}_{17}$), porous metal oxides ($\text{H}_4\text{Nb}_6\text{O}_{17}$) and the topotactic dehydrated porous metal oxides (Nb_6O_{15}). The surface

morphologies of the porous metal oxides and topotactic dehydrated porous metal oxides were characterized using scanning electron microscopy (S-4800, Hitachi, Japan) and transmission electron microscopy (TEM, Zeiss EM-10, Oberkochen, Germany). The band gap of the porous material was measured by using reflectance UV-visible scanning spectrophotometry (Shimadzu Kyoto, Japan). Surface areas, pore volume and pore sizes were measured using the Accelerated Surface Area and Porosity system (ASAP 2020) by Micromeritics Instrument Corporation (Georgia, USA). Lastly, the elemental analysis was done by Inductively Coupled Plasma – Optical Emission Spectroscopy (Optima 4300 DV, Perkin Elmer, Norwalk, CT, USA).

2.2.1. Transmission Electron Microscopy (TEM)

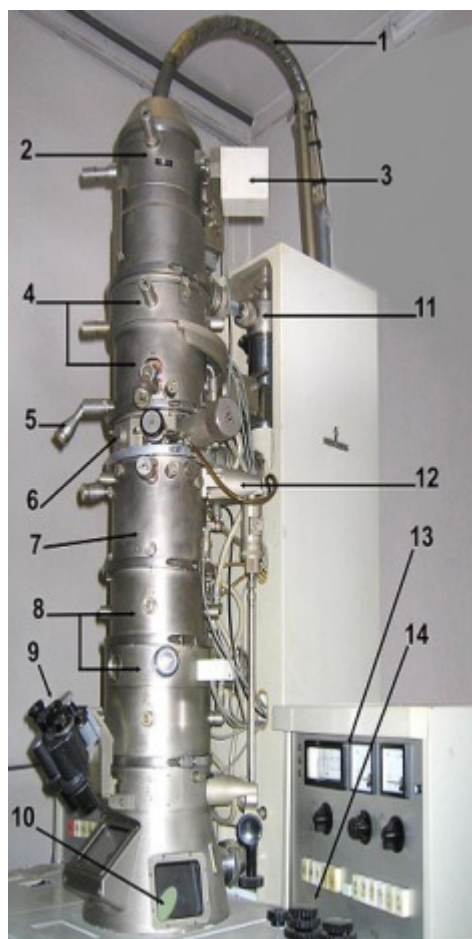
The transmission electron microscope (TEM) works on the same basic principle as the light microscope but it uses electrons instead of light. It may yield information such as ultrastructure, crystallographic information and compositional information (if so equipped).

The beam of electrons is transmitted through an ultra-thin specimen, interacting with it, while passing through it. An image is formed from this interaction and the image is magnified and focused onto an imaging device. The imaging device can be a fluorescent screen, or a layer of photographic film, or a sensor like a charged-coupled device (CCD) camera.

A transmission electron microscope has significantly high resolution due to the small De Broglie wavelength of the electron. This helps users examine fine details of their sample. A TEM is composed of several components such as a vacuum system in which the electron travels an electron emission source for generation of the electron beam, electromagnetic lenses and electrostatic plates. Figure 2.13 shows a typical TEM and its parts. Imaging devices are used to create images from the electron exit system. Imaging systems in a TEM consist of a phosphor screen, which may be made of fine (10-100 μm) particulate zinc sulphide, for direct observation

by the operator. An image can be recorded by some systems such as film based or doped YAG screen coupled CCDs. Typically these devices can be removed or inserted into the beam path by the operator as required.

Transmission electron microscopy of the colloid, porous metal oxides ($\text{H}_4\text{Nb}_6\text{O}_{17}$) and topotactic dehydrated porous metal oxides material (Nb_6O_{15}) were done using TEM system (TEM, Zeiss EM-10, Oberkochen, Germany) in the Analytical Cytology Core Facility, Border Biomedical Research Center, Department of Biological Sciences at UTEP. The TEM samples were prepared by diluting the samples in DI water and then placing them on Formvar-coated 200 mesh copper grids.



1. tension cable
2. Electron emitter (Tungsten filament)
3. Stepper motors for centering the electron beam
4. Condenser
5. Aperture High control
6. Specimen holder
7. Objective lens
8. Projector lens
9. Optical binoculars
10. Fluorescent screen
11. Vacuum pump leads
12. Goniometer (not on UTEP TEM)
13. Vacuum and magnification control
14. Focusing control

Figure 2.13: Transmission Electron Microscope.³⁷

2.2.2. Scanning Electron Microscopy (SEM)

A scanning electron microscope images the sample's surface by scanning it with a beam of high energy electrons. These electrons interact with the sample, thereby producing the signals which report the sample's properties. In standard detection mode, the secondary electron imaging (SEI) device produces very high resolution images of the sample surface.

The electron beam is emitted from the electron gun. This electron beam typically has the energy of 0.5 keV to 40 keV. The beam passes through pairs of scanning coils or deflector plates in the electron column and finally to the final lens, which deflects the beam in the x and y axes (Figure 2.14). This process makes the beam raster over a triangular area of the sample surface.

The morphologies of the porous metal oxides and topotactic dehydrated porous metal oxides were studied by using a shared scanning electron microscope system, located in the Department of Metallurgical and Materials Engineering at UTEP. This technique helped in studying and comparing the surface morphologies of the porous metal oxides.

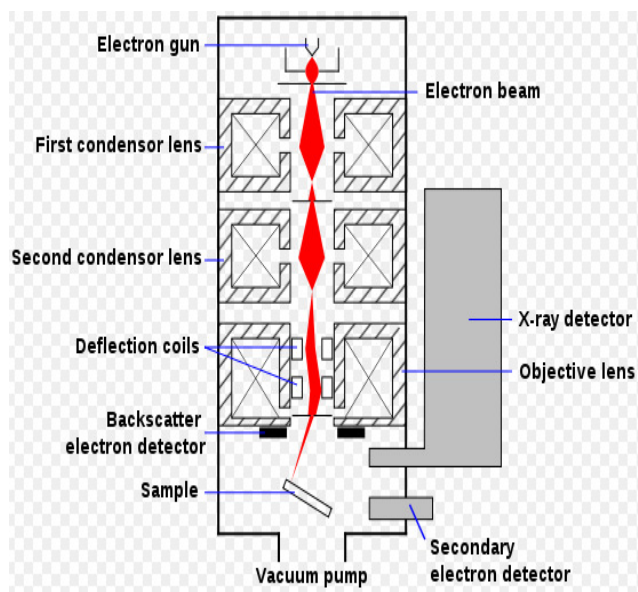


Figure 2.14: Scanning Electron Microscope.³⁸

2.2.3. X- ray Diffraction (XRD)

XRD works with the following principle. The atomic planes in a crystal cause an incident beam of monochromatic x-rays to interfere with one another as they leave the crystal. This phenomenon is called as X-ray diffraction. X-rays are produced whenever high speed electrons collide with a metal target.

English physicists, Sir W. H Bragg and his son Sir W. L Bragg developed a process in 1913 explaining that the cleavage faces of the crystal appear to reflect the x-ray beam at certain angles of incidence (theta, θ). They proposed a law, which came to be known as Bragg's Law:

$$n\lambda = 2d\sin\theta \quad \text{where, } n = \text{an integer}$$

λ = wavelength of x-ray beam

d = distance between atomic layers in a crystal

θ = angle of incidence.

This observation gave an example of X-ray wave interference; commonly known as X-ray diffraction (XRD), which provided direct evidence for the periodic atomic structure of the crystals.

XRD has many applications as listed below:

1. To identify the crystalline phases and orientation.
2. To determine atomic arrangement and the structural properties such as lattice parameters, phase composition and thermal expansion.
3. To measure the thickness of films and multilayers.

XRD is very efficient in sample characterization as it is a non-destructive and sample preparation is fast and easy. XRD gives high accuracy for d-spacing calculations. It can be done

in-situ. It can work for single, polycrystalline or amorphous materials. Also, standards are available for thousands of material systems.

For my research, the degree of crystallinity of the porous metal oxides was measured with an X-ray diffractometer (Cu-K α) in the Department of Metallurgical and Materials Engineering at UTEP. XRD was carried out for Parent material (K₄Nb₆O₁₇), unexfoliated material (acid exchanged H₄Nb₆O₁₇), porous metal oxides material (H₄Nb₆O₁₇) and topotactic dehydrated material (Nb₆O₁₅). Samples were prepared by placing around 100 mg of the sample in a 20 mm center hole of a 2 mm thick aluminum plate. The scanned angles ranged from 5° to 80° 2 θ .

2.2.4. X-ray fluorescence spectroscopy (XRF)

XRF is a non destructive method for chemical analysis of elements. An X-ray or gamma ray source is used to irradiate the material to emit their characteristic X-rays. A detection system, which is wavelength dispersive, is used to measure the peaks of the emitted x-rays for the measurement of the element and their amounts. XRF can be simultaneously used to determine the elemental composition and film thickness.

The process begins by exposing the sample to a source of X-rays or gamma rays. The high energy photons strike the sample, knock the electrons out of their orbitals around the nuclei of the atom, which make up the sample. During this time, an electron from the outer shell of the atom will fall to the shell of the missing electron. Since the outer shell electrons are more energetic than the inner shell electrons, the electron falling in to the lower shell has excess energy which is emitted as an X-ray photon. The detector collects the photons and converts them to electrical impulses that are directly proportional to the energies of the various x-rays in the samples' spectrum (Figure 2.15).

For the characterization, XRF spectroscopy was used on the porous metal oxides ($\text{H}_4\text{Nb}_6\text{O}_{17}$) and topotactic dehydrated porous metal oxides (Nb_6O_{15}). XRF was done on a XDAL, Fischerscope X-ray system (Vastra Frolunda, Sweden) housed in Dr Gardea's laboratory in the Department of Chemistry at UTEP.

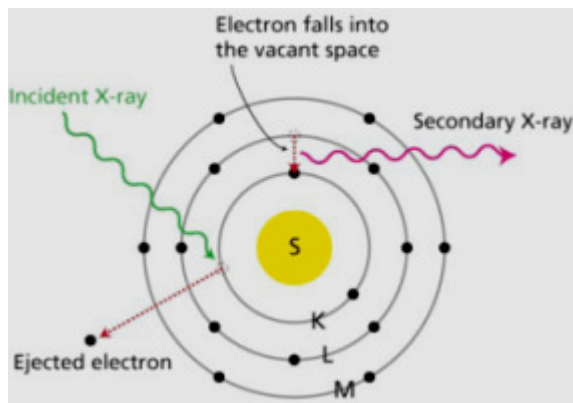


Figure 2.15: Production of secondary X-rays in XRF.³⁹

2.2.5. Accelerated Surface Area and Porosimetry System

Knowledge of the surface area and pore size distribution is crucial for the fundamental studies of molecular adsorption and transport in the nano porous solids. It is an essential tool for providing surface area and porosity measurements and for providing a broad range of research development and quality control applications.

The Accelerated Surface Area and Porosimetry System (ASAP 2020) analyzer has two independent vacuum systems, one for sample preparation and another for sample analysis. This independent vacuum system allows the preparation and analysis to proceed concurrently without any delay. Compressed gases (nitrogen and helium) are used in the analysis.

The Brunauer-Emmett-Teller (BET), Langmuir surface areas and pore volumes of the metal oxide aggregates of hexaniobate were calculated from the nitrogen adsorption-desorption

isotherms at 77 K obtained on the ASAP 2020. Pore sizes and pore size distributions were determined using the Barrett-Joyner-Halenda (BJH) model assuming a cylindrical geometry. Before the BET measurement, the catalyst was degassed with nitrogen at 90 °C under vacuum for two and half hours and backfilled with nitrogen or helium gas to remove excessive moisture or adsorbed contaminants from the surface of the sample. Degassing was followed by analysis, which took about 10 hours. The obtained data was calculated by the various models in the computer aided system.



Figure 2.16: The ASAP 2020 (Micromeritics) surface area analyzer (BET).⁴⁰

Analysis Technique

The basics of the analytical technique used in these porosity systems are simple. A sample contained in an evacuated sample tube was cooled in liquid N₂, and then was exposed to the analysis gas at a series of precisely controlled pressures. With each incremental pressure increase, the number of gas molecules adsorbed on the surface increases. As adsorption proceeded, the thickness of the adsorbed film increased. Any micropore in the surface was quickly filled, then the free surface became completely covered, and finally larger pores were filled. Then the desorption process began, in which pressure was systematically reduced resulting in the liberation of adsorbed molecules. As with the adsorption process, the changing amount of gas on the solid surface was quantified by monitoring the pressure.

Sample Preparation for ASAP 2020 Porosity System

An empty long stem sample tube was first weighed and then a dried sample of known quantity (0.06 g) was placed in the sample tube. This sample tube with the sample was weighed again. Then, the weight of empty sample tube was subtracted from the later which gave the net weight of the sample. A sample tube was plugged into a degassing port and a heating mantle was attached to it. The parameters for degassing, adsorption, analysis and final report were chosen, and the analysis was started. The BET and Langmuir surface area, pore volumes, pore sizes, and pore size distribution of the porous metal oxide aggregates of hexaniobate were measured.

Degassing Conditions used for the Evacuation and Heating Phase

Pretreatment of the porous materials was done to each sample in a degassing process. The non topo porous material (H₄Nb₆O₁₇) and topotactic dehydrated porous material (Nb₆O₁₇) were characterized.

The typical parameters chosen for all samples were as follows:

The temperature ramp rate: 10 °C /min;

The target temperature: 90 °C;

Evacuation rate: 5 mm Hg/s;

The unrestricted evacuation began from 5 mm Hg/s;

Vacuum set point: 100 µm Hg;

Evacuation time: 30 min.

The ramp rate for the heating phase: 10 °C /min;

The holding temperature: 120 °C for two hours;

Figure 2.17 shows the parameters for degassing.

The screenshot displays the 'ASAP 2020 V1.04' software window with the file path '[C:\2020\TRAINING\000-054.SMP]'. The 'Degas Conditions' tab is active, showing the following parameters:

Evacuation Phase	
Temperature ramp rate:	10.0 °C/min
Target temperature:	90 °C
Evacuation rate:	5.0 mmHg/s
Unrestricted evac. from:	5.0 mmHg
Vacuum setpoint:	10 µmHg
Evacuation time:	30 min

Heating Phase	
Ramp rate:	10.0 °C/min
Hold temp:	150 °C
Hold time:	120 min

Evacuation and Heating Phases	
Hold pressure:	100 mmHg

At the bottom, there is a checkbox labeled 'Backfill sample tube' which is checked.

Figure 2.17: Parameters for degassing the porous metal oxides in ASAP 2020 porosity system.

Before analysis, a tube containing a sample was weighed and subtracted from weight of empty sample tube to determine any weight loss. If there is any weight loss, we put the last number as

the sample weight. The parameters needed for the analysis of surface area, pore volume and pore sizes are as follows:

The relative pressure range (p/p_0): 0.05 to 0.3;

Backfill gas: Nitrogen gas.

After the degassing process was complete, the sample tube was removed from the degassing port and plugged into the analysis port in order to run the samples in the analysis phase. Figure 2.18 shows the parameters for analyzing porous aggregates.

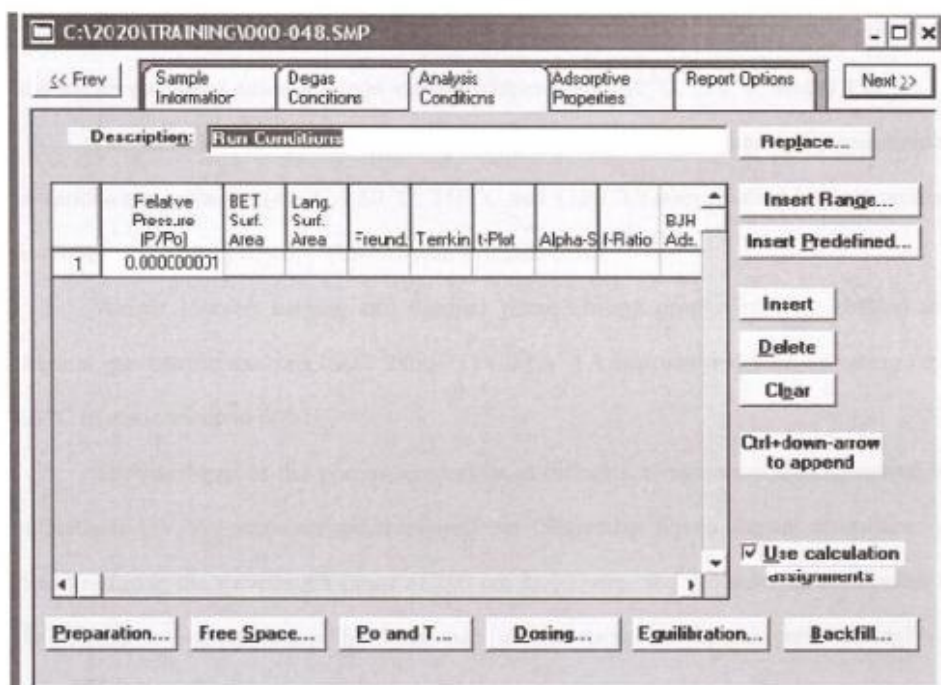


Figure 2.18: Parameters for analyzing the porous aggregates samples in ASAP 2020 porosity.

2.2.6. Inductively Coupled Plasma – Optical Emission Spectroscopy (ICP-OES)

ICP-OES is an analytical technique used for the detection of trace metals. It uses inductively coupled plasma to produce excited atoms and ions that emit electromagnetic radiations at wavelengths characteristic of a particular element in question. The intensity of the emission is proportional to the concentration of the element in the sample.

The ICP-OES is divided into two parts; one is the ICP and the other is the optical spectrometer. The ICP torch consists of 3 quartz tubes which is partly surrounded by an output coil of the radio frequency generator (Figure 2.19). When the torch is turned on, an electromagnetic field is created within the coil. The argon gas flowing through the torch is ignited with the Tesla unit, thereby creating a brief arc through the argon flow which initiates the ionization process. After the plasma is ignited, the Tesla unit is turned off.

A sample is introduced in the core of the ICP, which is at a temperature of approximately of 8000 °C. All the elements become thermally excited and emit light at a wavelength, characteristic of the particular element. The spectrometer collects this light and passes it through a diffraction grating, which serves to resolve the light into the spectrum of its constituent wavelengths. This diffracted light is then counted into an electrical intensity measurement, which can be converted to an elemental concentration by comparing with the calibration standards.

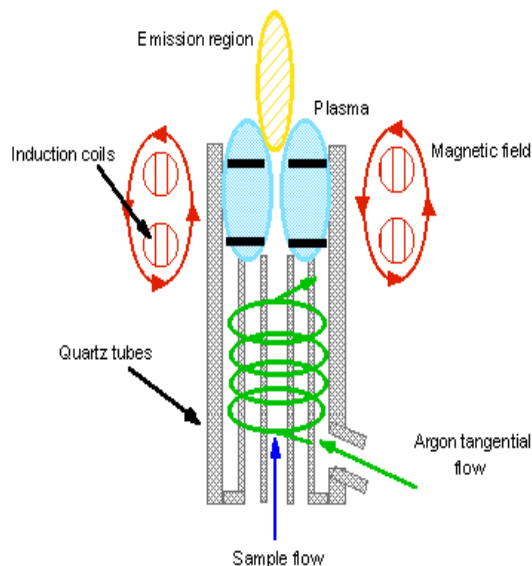


Figure 2.19: ICP-OES, Torch for Trace element detection.⁴¹

2.2.7. UV – visible Scanning Spectrophotometer

The instrument used in the ultraviolet-visible spectroscopy is called the UV/vis spectrophotometer. It is the measurement of the attenuation of the beam of light after it passes through a sample or after reflection from a sample surface. Absorption measurement can be a single wavelength or over an extended spectral range.

The basic parts of a spectrophotometer are a light source, sample holder, a diffraction grating or monochromator to separate different wavelengths of light, and a detector (Figure 2.20). The radiation source is often a halogen lamp filament (300-2500 nm), a deuterium arc lamp which is continuous over the ultraviolet region (190-400 nm), and more recently light emitting diodes (LED) and xenon arc lamps for the visible wavelengths. The detector is typically a photodiode or a charge-coupled device (CCD). Photodiodes are used with monochromators, which filter the light so that only light of a single wavelength reaches the detector. Diffraction gratings are used with CCDs, which collect light of different wavelengths on different pixels.

A spectrophotometer can be either single beam or double beam. In a single beam instrument all of the light passes through the sample cell. The intensity of the incident light at a given wavelength must be measured by removing the sample. This was the earliest design, but is still in common use in both teaching and industrial laboratories. In a double-beam instrument, the light is split into two beams before it reaches the sample. One beam is used as the reference; the other beam passes through the sample. Some double-beam instruments have two detectors (photodiodes), and the sample and reference beam are measured at the same time. In other instruments, the two beams pass through an optical chopper, which blocks one beam at a time.

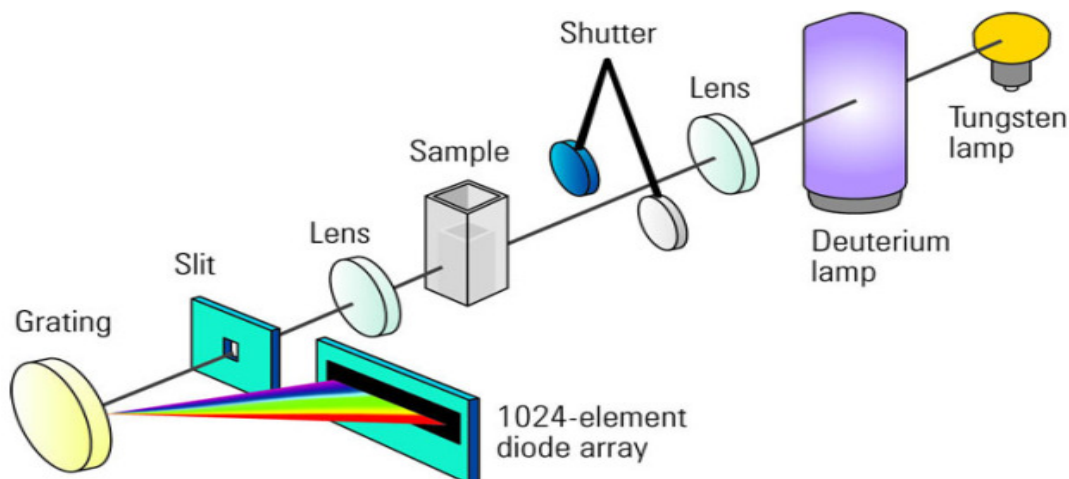


Figure 2.20: Working of the UV-Vis Spectrophotometer.⁴²

Samples for UV/vis spectrophotometry are most often liquids, although the absorbance of gases and even of solids can also be measured. Samples are placed in a transparent cell, known as a cuvette. Cuvettes are typically rectangular in shape, commonly with an internal width of 1 cm. The type of sample container used must allow radiation to pass over the spectral region of interest. The most widely applicable cuvettes are made of high quality fused silica or quartz glass because these are transparent throughout the UV, visible and near infrared regions. Glass and plastic cuvettes are also common, although glass and most plastics absorb in the UV, which limits their usefulness to visible wavelengths.

UV-Vis Spectrophotometer Accessories (Solid Samples)

Since light cannot penetrate opaque (solid) samples, it is reflected from the surface of the samples. The incident light reflected symmetrically with respect to the normal line is called specular, while the incident light scattered in different directions is called diffuse reflection. Diffuse reflection including specular reflection can be measured by using an integrating sphere. The sample is placed in front of the incident light window and the light is concentrated from the

sample to the detector using a barium sulfate coated sphere. The value, thus obtained becomes the reflectance with respect to the reflectance of the reference standard (which is taken to be as 100%). As the light is directed on the sample, the specular reflected light exits the integrating sphere and is not detected. Hence, only the diffuse reflected light is measured.

2.3. Results And Discussions

2.3.1. TEM Images

The TEM images of the colloid show aggregates of sheets, which are folded and wrinkled which leads to the random porosity of the material (Figure 2.21a-b). In the case of non-topo POX, the sheets had rolled up and formed nano scrolls (Figure 2.22a-b). The average length of the tubules was found to be 440 nm and the average diameter was found to be 29 nm. It is interesting to note that, some of the sheets have not rolled to form tubules as seen in Figure 22 (a). The TEM images of topo POX show that there is some kind of decomposition in the material (Figure 2.23a-b). The tubules are not as smooth as non-topo tubules. The average length and diameter of the tubules was the same as in the non-topo POX (440 nm and 29 nm respectively).

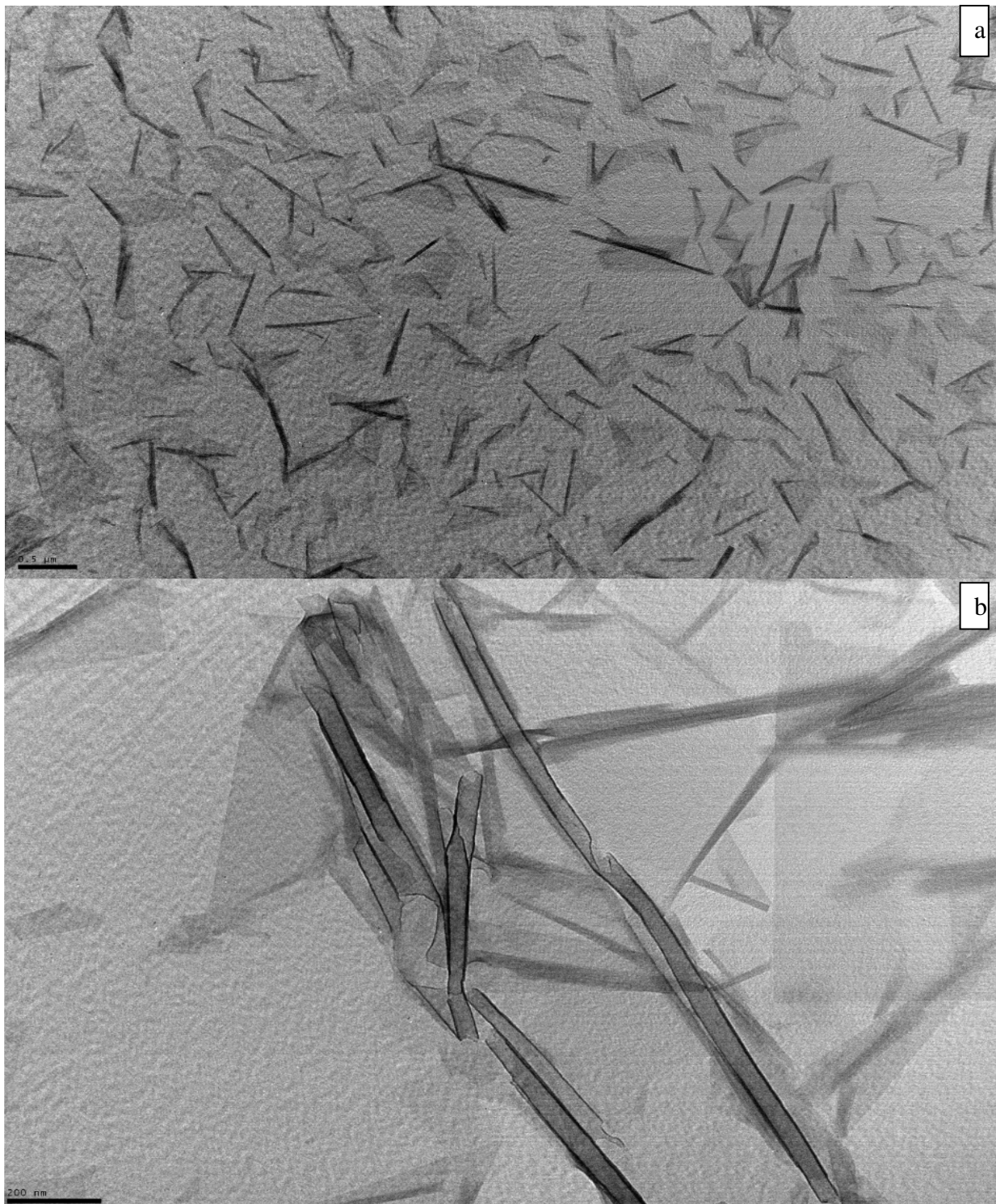


Figure 2.21 a-b: TEM images of colloid material.

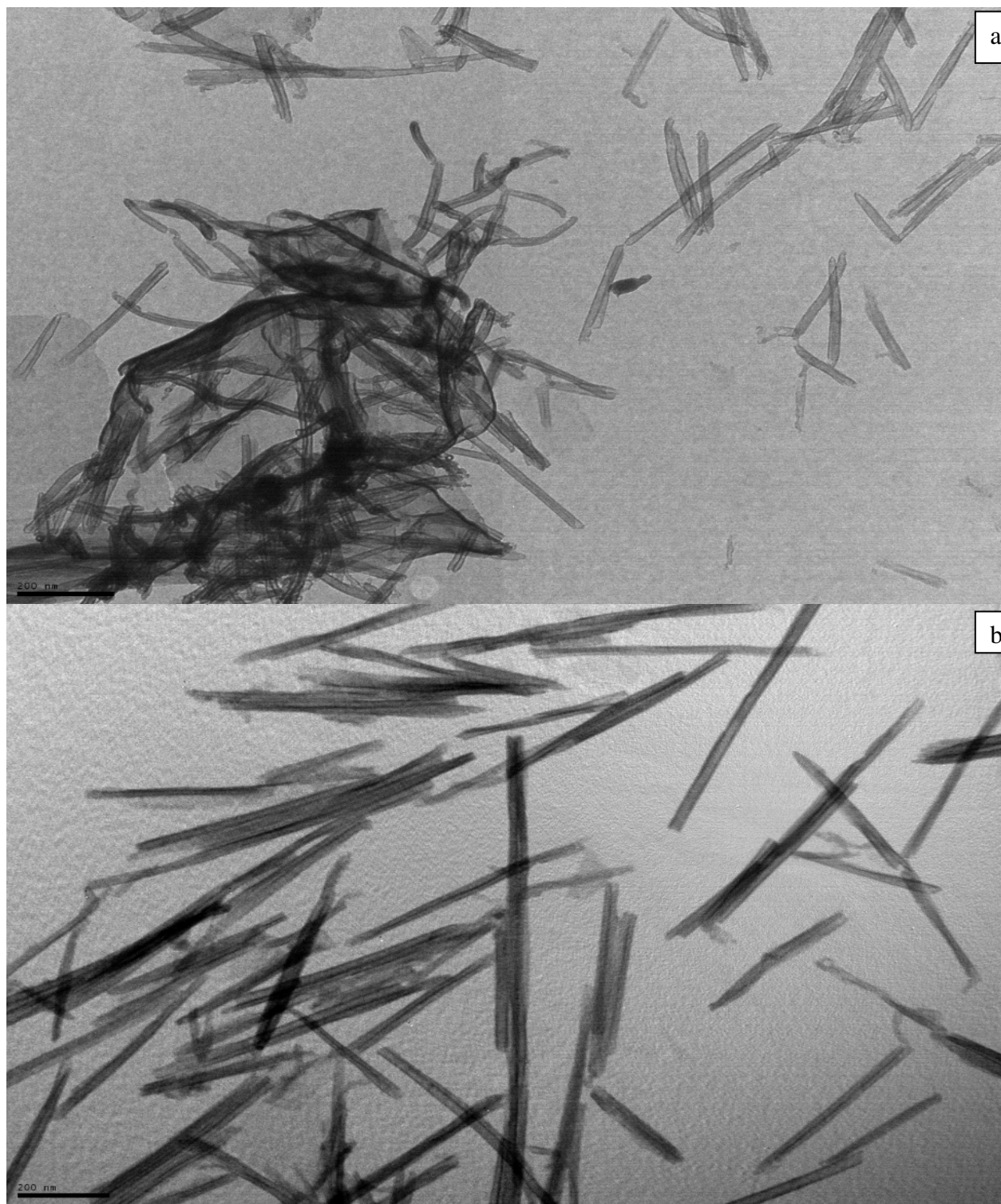


Figure 2.22 a-b: TEM images of non-topo POX ($\text{H}_4\text{Nb}_6\text{O}_{17}$).

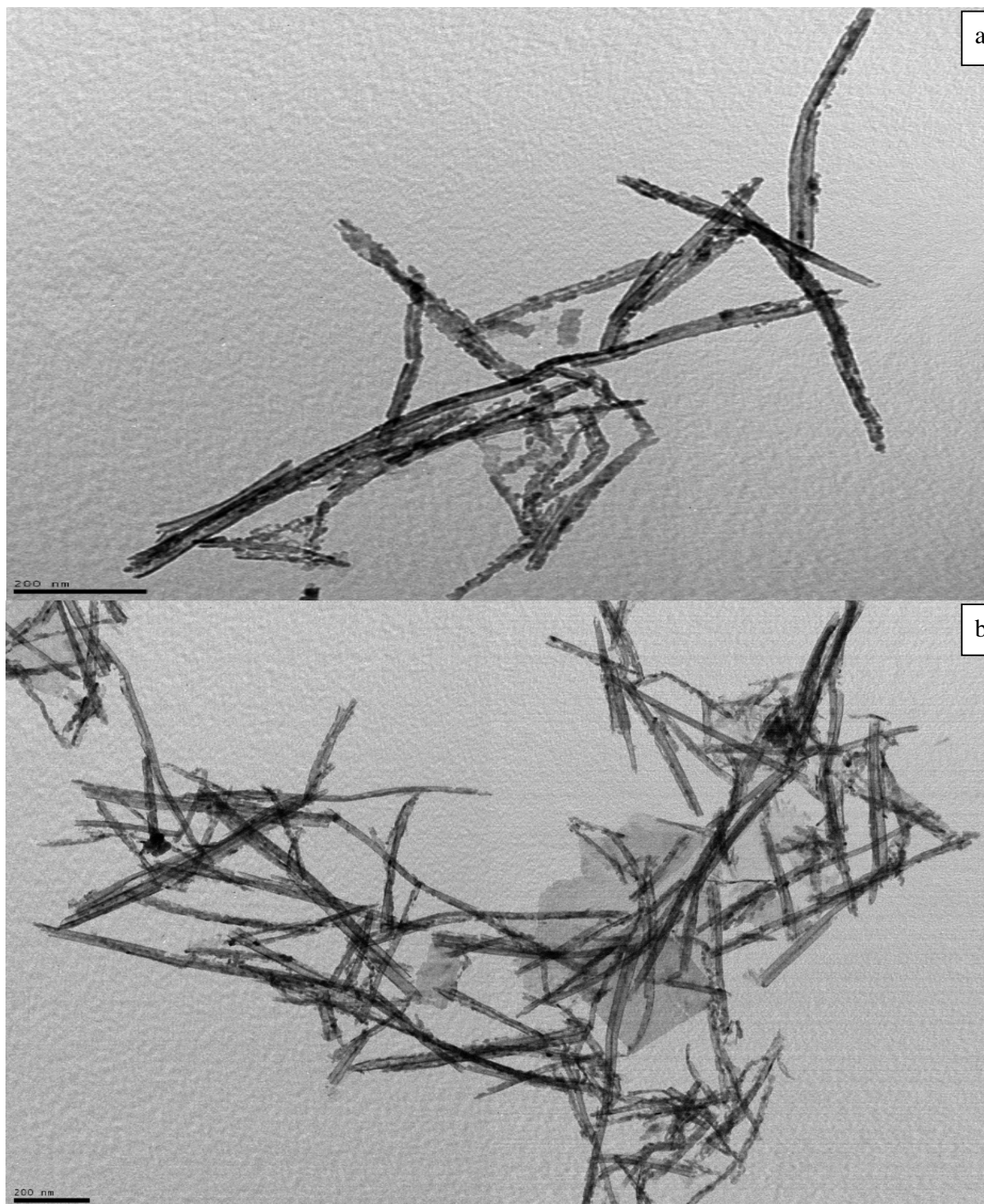


Figure 2.23a-b: TEM images of topotactic dehydrated POX (Nb_6O_{15}).

2.3.2. SEM Images

The morphology of non-topo and topo POX were studied using scanning electron microscopy.

Figures 2.24a, b and c show SEM images of non-topo POX materials. They show the existence of high porosity and homogeneity throughout the sample. In Figures 2.24a and b, one can notice the open ends of the nano tubules. Figures 2.25a, b and c show the SEM images of the topotactic dehydrated metal oxides. The images show that the tubules have slightly decomposed and have become rugged. The smoothness of the non-topo materials is lost in the topo materials. Nonetheless, the porosity is maintained.

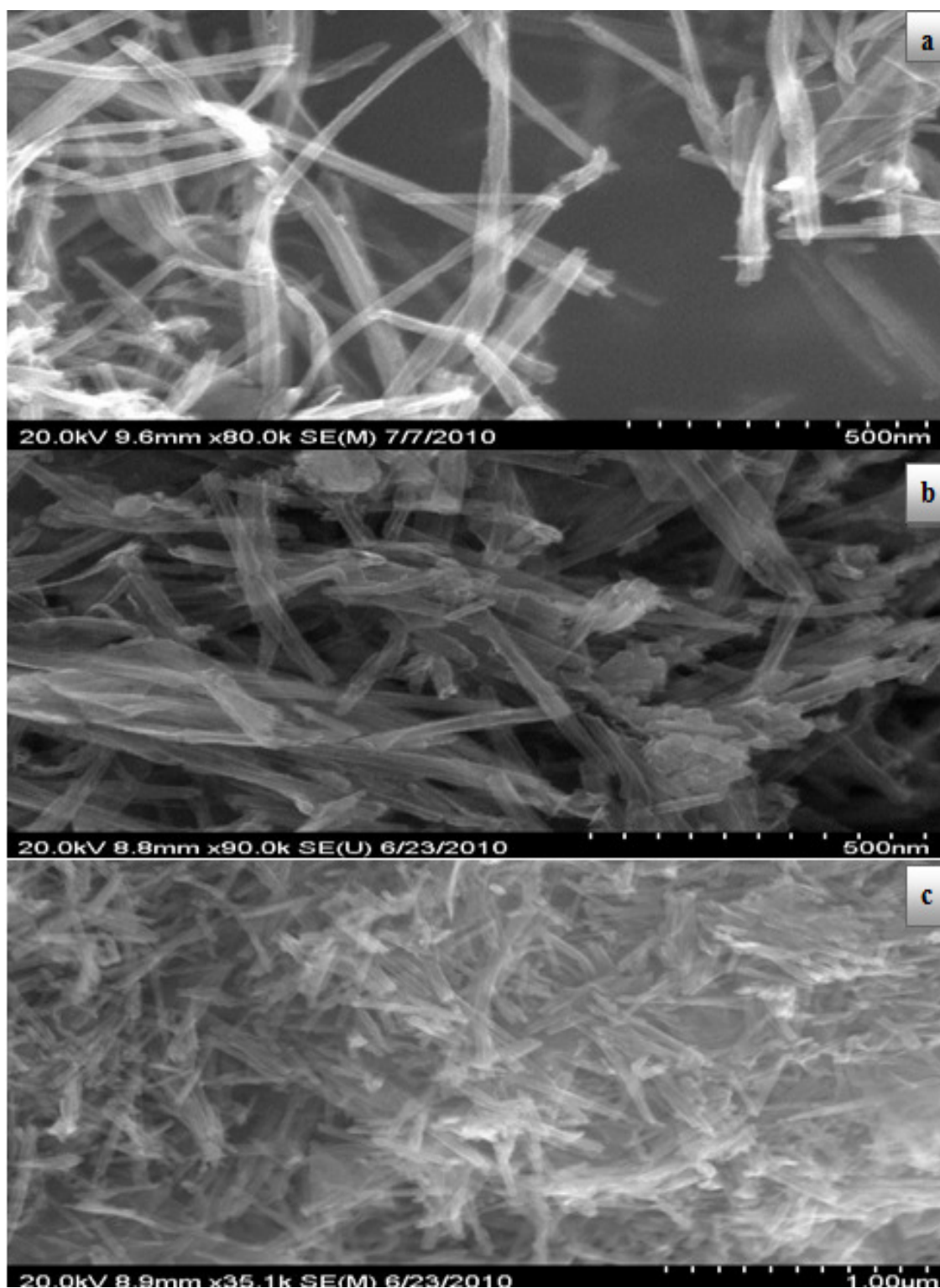


Figure 2.24a, b and c: SEM images of non-topo POX material ($\text{H}_4\text{Nb}_6\text{O}_{17}$).

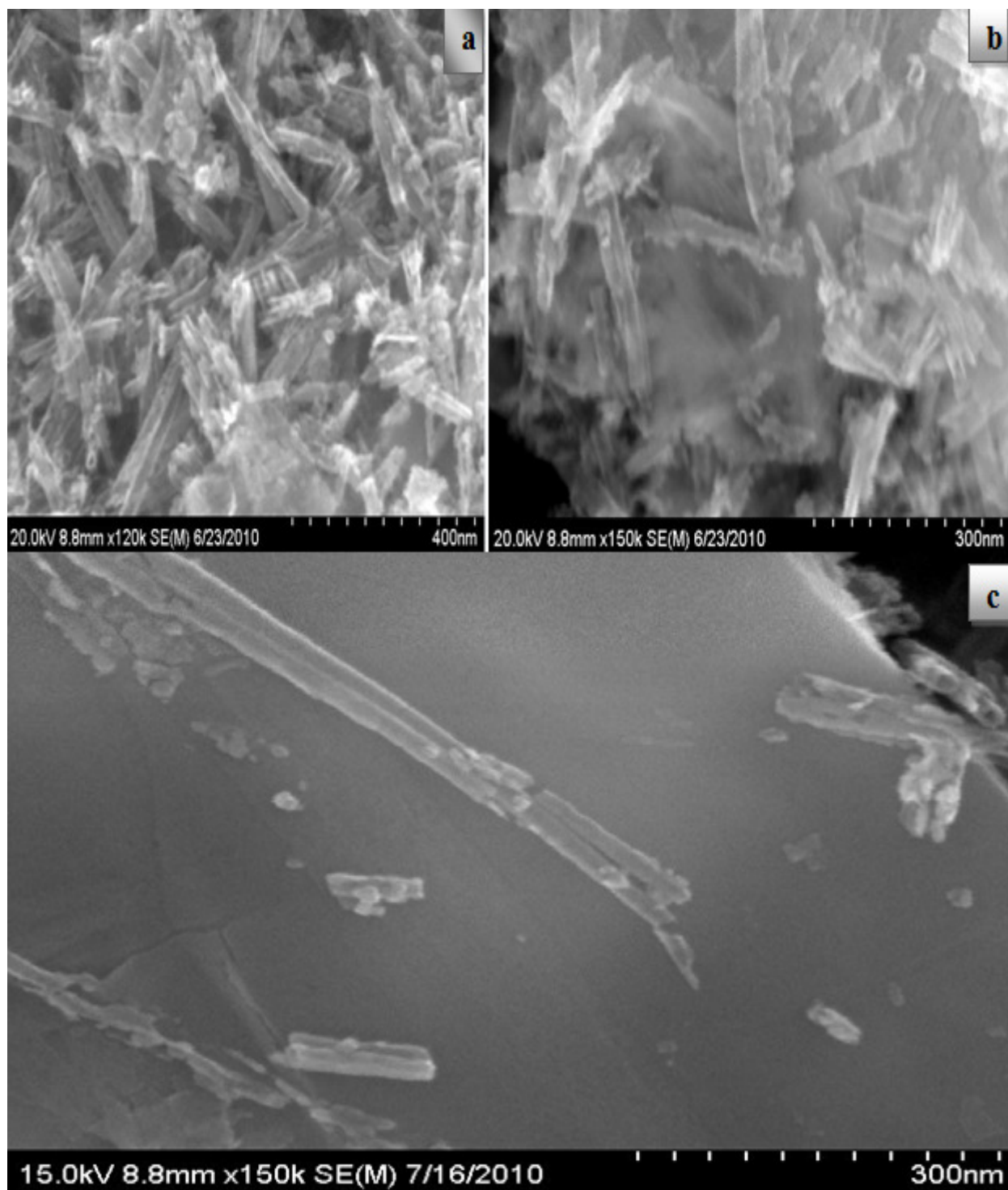


Figure 2.25a, b and c: SEM images of topotactic dehydrated POX material (Nb_6O_{15}).

2.3.3. XRD Patterns of the Porous Metal Oxides

The crystal structures and XRD patterns of the parent material ($\text{K}_4\text{Nb}_6\text{O}_{17}$), acid exchanged material, non topo hexaniobate and topotactic dehydrated hexaniobate were studied using X-ray powder diffraction. Diffractograms are shown in Figure 2.26.

For the parent and acid exchanged material, high crystallinity was observed. The first intense peak for the parent material and acid exchanged material at 2θ around 10° corresponds to the interlayer spacing of the sheets. The peak for acid exchanged material has moved slightly to the right, indicating that the d-spacing between the layers has decreased. This could be due to the replacement of the larger potassium ions by smaller protons.

The XRD pattern of the nanotubule porous aggregates of the non-topo and topo POX show poor periodic layer structures as compared to parent and acid exchanged materials. It also shows a lower degree of crystallinity (as compared to those of the parent and acid exchanged materials).

The reason for the loss of diffraction peaks in the non-topo and topo aggregates is due to the random orientation of the restacked tubules and loss of periodicity. Once the parent materials are exfoliated, the sheets lose contact with each other and do not align in a regular manner. When the sheets are restacked together, there is no regular contact between the sheets, but they are randomly aligned. However, the small peak present on the XRD pattern of the non-topo material demonstrates that there is still some kind of periodicity, maybe from poorly organized restacking layers. This layered peak is non-existent in the topotactic dehydrated hexaniobate. This is due to a dehydration reaction and removal of interlayer protons that occurs in these materials at elevated temperature.

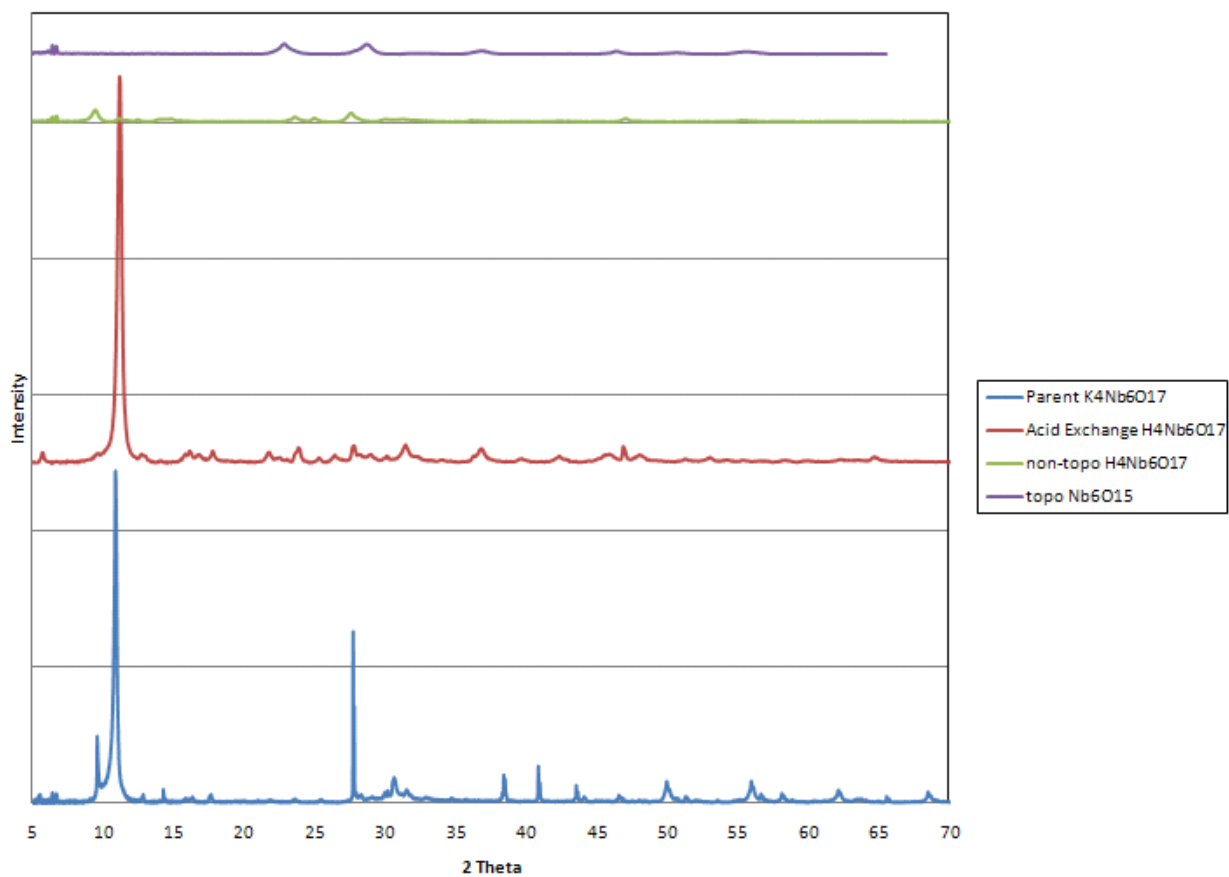


Figure 2.26: XRD patterns of parent material $K_4Nb_6O_{17}$, acid exchanged $H_4Nb_6O_{17}$, non-topo ($H_4Nb_6O_{17}$) and topo (Nb_6O_{15}).

2.3.4. X-ray Fluorescence Spectrometry (XRF)

X-ray fluorescence spectrometry of non-topo and topo POX was done (XDAL, Fischerscope X-ray system). Both the materials showed the presence of niobium (Figure 2.27a and b). XRF was used to see if samples contained any potassium residues from the parent compounds, $K_4Nb_6O_{17}$. The data show no potassium was present. However, the limits of the XRF do not rule out the trace amounts of potassium. See data in section on ICP-OES analysis.

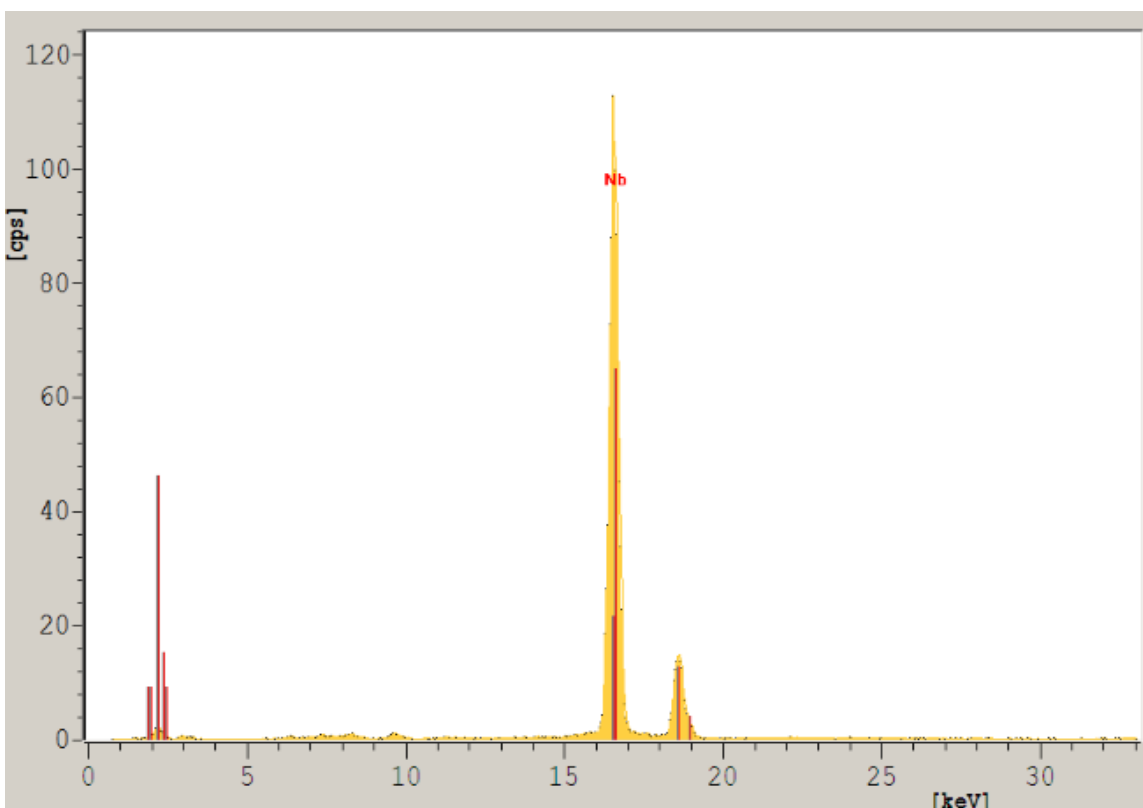


Figure 2.27a: Typical X-ray fluorescence data for of POX (non-topo) samples.

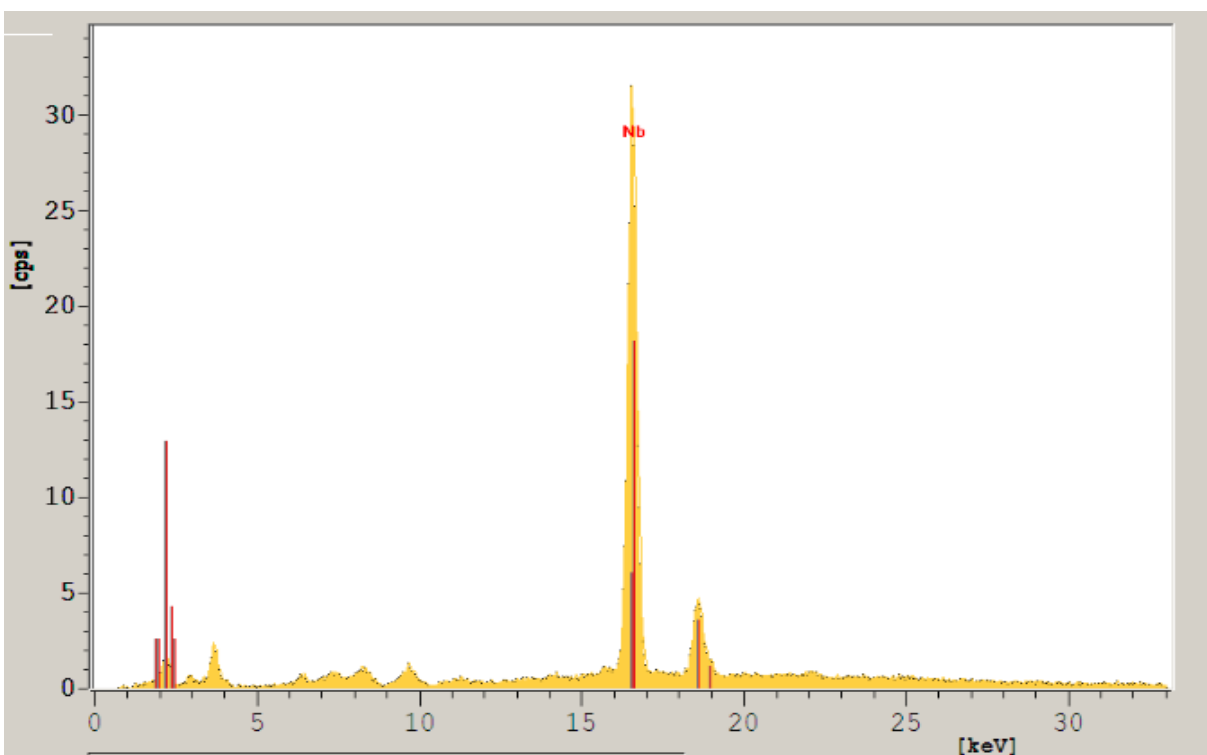


Figure 2.27b: Typical X-ray fluorescence data for POX (topo) samples.

2.3.5. BET Surface Area and Pore Analysis of Porous Metal Oxides

Figure 2.28 shows the pore volume measurements for the pores of non topo POX ($\text{H}_4\text{Nb}_6\text{O}_{17}$), while Figure 2.29 shows the pore volume measurements for the pores of topo POX (Nb_6O_{15}). The pore size distribution was random for both the materials and majority of the pore volumes were coming from very large pores. Irrespective of having random pore size distribution, both the materials have two common peaks at 35 Å and 80 Å (Figures 2.28 and 2.29). It is speculated that folding of the sheets may cause the peak at 35 Å. The peak at 80 Å may correspond to the inner diameter of the tubes.

The non-topo POX was found to have the BET surface area of 172 m²/g with an average pore diameter of 87 Å. The topo POX was found to have the BET surface area of 148 m²/g with an average pore diameter of 93 Å (Table 2.1). It is apparent that the specific surface area decreases when the samples were heat treated.

Table 2.1: BET surface area measurement for non-topo and topo POX

Sample	Single point surface area, (m ² /g)	BET surface area, (m ² /g)	Langmuir surface area, (m ² /g)	BJH desorption pore volume, (cm ³ /g)	BJH desorption Average pore Diameter, Å
H₄Nb₆O₁₇ (Non-topo)	166.18	171.99	272.99	0.40	87.00
Nb₆O₁₅ (Topo)	143.75	148.44	236.11	0.14	92.80

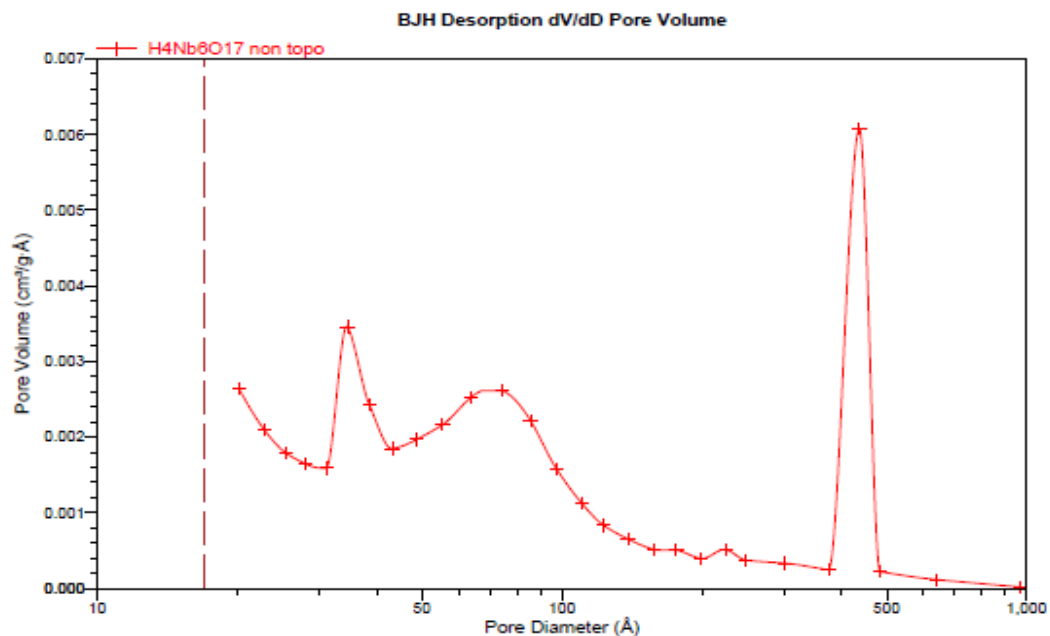


Figure 2.28: BJH Desorption dV/dD Pore Volume of non-topo POX.

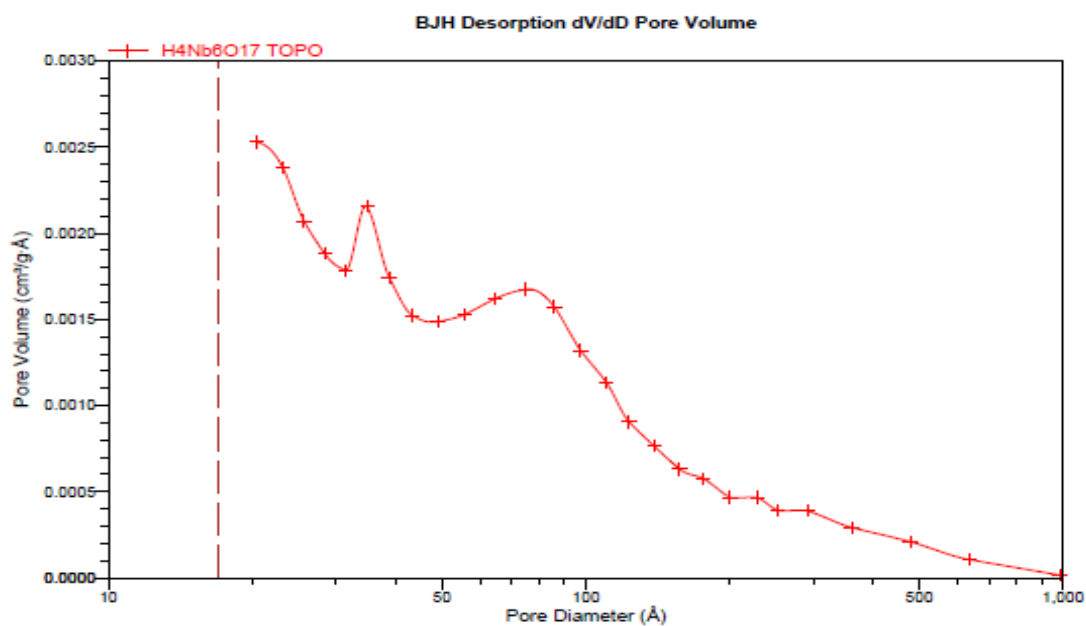


Figure 2.29: BJH Desorption dV/dD Pore Volume of topo POX.

2.3.6. ICP-OES analysis

The result in Table 2.2 shows the presence of niobium and potassium in the sample. Though, there were five batches of consecutive acid exchanges done to remove potassium, yet, there is still some potassium remaining in the sample.

Table 2.2: ICP-OES analysis of topotactic dehydrated hexaniobate porous metal oxides.

Type of Sample	K (ppm)	Nb (ppm)
$\text{H}_4\text{Nb}_6\text{O}_{17}$	0.12	2.65

2.3.7. UV – visible Reflectance Spectrometry

The band gap of hexaniobate materials were measured for acid exchanged, non-topo POX and topotactic dehydrated POX by using a UV-vis scanning spectrophotometer. The onset of absorption was determined by extrapolating the steep part of the rising absorption curve and wavelength (Figure 2.30). The onset of absorbance is energy where electrons and holes separate from each other. At this point, the light starts to be absorb and band gap energy is calculated using the equation $E=hc/\lambda$, where c is the speed of light (2.99×10^8 m/s), h is Plank's constant (6.626×10^{-34} J/sec) and λ is the wavelength. The onset of absorption of hexaniobate samples was extrapolated and the energy band gap for each one of them was calculated. This is shown in Table 2.3.

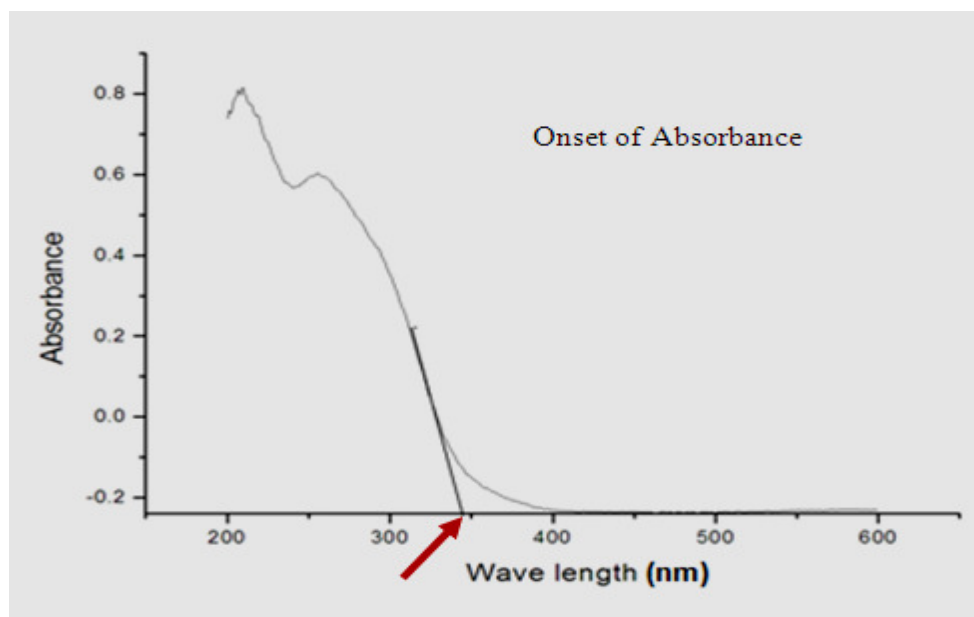


Figure 2.30: Determination of onset of absorbance.

Table 2.3: Onset of absorbance and energy band gap for hexaniobate metal oxide.

Sample	Absorbance onset for hexaniobate (nm)	Energy bandgap (eV) $E=hc/\lambda$
Acid exchanged	360	3.447
Non-topo POX	355	3.495
Topo POX	389	3.189

The energy band gap for the non-topo porous metal oxides was found to be the largest as compared to the acid exchanged and toptacttic dehydrated materials. There was a blue shift in the spectra of the non-topo material as compared to the acid exchanged compound (Figure 2.31). This blue shift may be due to the new morphology and structure of the materials. In the acid exchanged materials, the sheets are stacked tightly together, making up a layered material. On comparing non-topo porous metal oxide tubules with acid exchanged materials, the non topo material behaved like a nano particle composite. Nanoparticles of sufficiently small dimensions

are known to induce a blue shift in their spectra compared to the bulk samples. The absorption edge at about 360 nm in the acid exchanged material turned to lower wavelength of 355 nm for non-topo materials. For the topotactic dehydrated metal oxides, the absorption edge was around 389 nm, which is the highest of the three materials measured. The removal of protons during topotactic dehydration caused the layered structure to become more three dimensional. This made the topo POX materials more bulk-like and hence, they absorbed lower energy. It is not clear how much of the changes in the photo physical properties are due to particle size change and how much is due to the chemical changes and crystal structure.

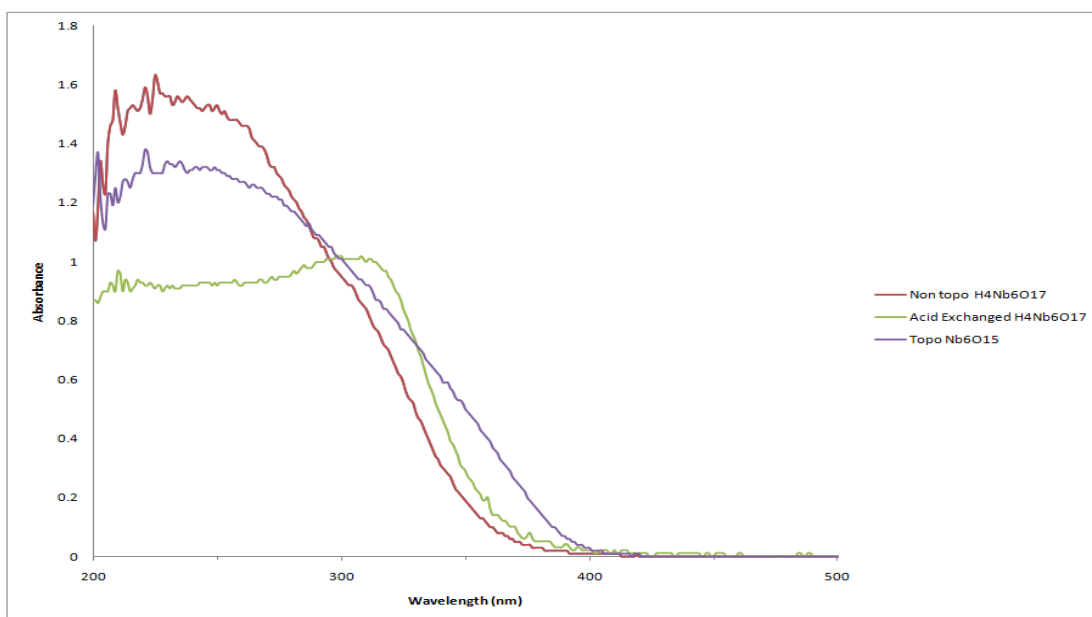


Figure 2.31: Absorbance data for the hexaniobate samples (parent materials, acid exchanged, non topo and topo POX).

Chapter 3: Hydrogen Production under Ultraviolet Light

3.1. Introduction

Platinum metal is often used as a co-catalyst in metal oxide photocatalytic systems. To investigate the photocatalytic activity of the new POX photocatalytic materials under ultraviolet light, platinum was photoreduced out of solution and deposited onto the surface of the non topo and topo POX. Metal reduction onto the surface of the POX material occurred during UV irradiation in the presence of the metal ions in solution. The amount of metal removed from the solution was considered to indicate the amount of metal deposited. Scanning electron microscopy and transmission electron microscopy were used to determine the particle size of the reduced metal and metal deposition patterns.

3.1.1. Experimental set up for metal deposition

Photochemical reduction was done by placing 0.015g of POX- $\text{H}_4\text{Nb}_6\text{O}_{17}$ (topo and non topo) and the required amount of an aqueous 100 ppm Pt solution (EM Science, USA, 1000 ppm standards), 0.2% nitric acid and anhydrous ethanol (Sigma- Aldrich, St. Louis, MO, USA) into a 16 cm long customized quartz tube. Table 3.1 below shows the amount of the reagents used for different metal loadings. The quartz tube containing the sample was then placed on a magnetic stirrer and then irradiated with a Penray (UVP LLC, USA) Hg light bulb (UV pen lamp, model 35C-9, rated $5.4 \text{ mW/cm}^2 @ 19 \text{ mm} @ 254 \text{ nm}$) at 20 mm distance (face of the bulb to face of the quartz tube).

Table 3.1: Different amounts of reagents for different percentages of metal loading onto the POX.

Metal Loading (%)	Amount of POX (g)	100 ppm of Pt standard (mL)	0.2% HNO₃ (mL)	Anhydrous Ethanol (mL)
0.5	0.015	0.75	29.25	1.0
1	0.015	1.5	28.5	1.0
2	0.015	3.0	27.0	1.0
5	0.015	7.5	22.5	1.0

Pt⁺⁴ metal ions K₂PtCl₆ were reduced to their metallic state and photodeposited onto the surface of the POX material. Non topo and topo POX were tested for their ability to reduce metal ions (Figure 3.1). POX samples and platinum solutions were irradiated under UV and periodically, 4 mL of the sample was withdrawn from the quartz tube and centrifuged. The liquid phase was separated and analyzed to determine the concentration of the unreduced metal. The solid phase was washed and rinsed twice with DI water and kept for analysis by scanning electron microscopy and transmission electron microscopy to determine the deposition pattern and preference of the metal on the POX material. The platinum deposited solid and the supernatant were both analyzed by ICP-OES.

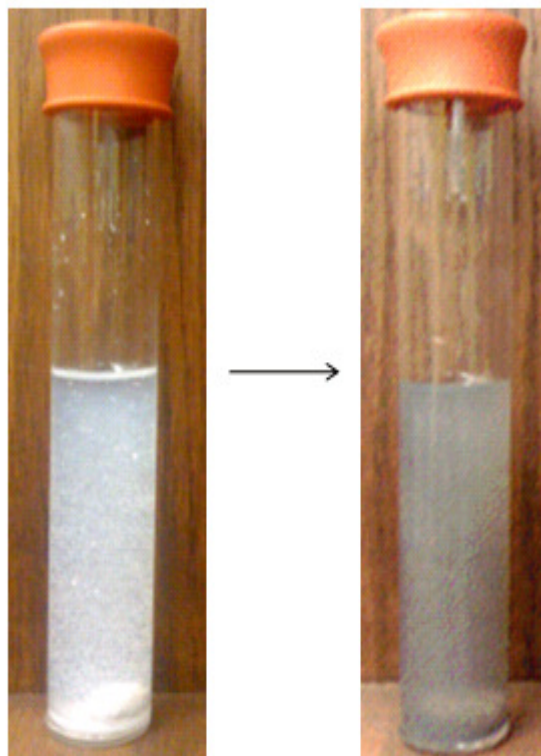


Figure 3.1: Quartz tube with A POX suspension inside showing reduction of metallic platinum on the material surface. After deposition, the color of the POX changed from white to grey.

3.1.2. SEM analysis of the metal deposited POX materials

Platinum deposited POX materials (non-topo and topo) were rinsed with DI water, dried in air and examined under a scanning electron microscope to determine the particle size distribution and deposition patterns.

Figures 3.2 (a-b) show the SEM images of non-topo POX materials, with platinum deposited on them. The platinum ions have been reduced and deposited onto the surface of the POX. The deposition pattern appears to be random. The average particle diameter of the platinum is around 20 – 55 nm.

Figures 3.3 (a-b) show the SEM images of topo POX with platinum deposited on them. The circles indicate what the Pt particles look like. It is interesting to find that not much platinum was deposited onto the surface of the topo POX materials. This may be due to the partial decomposition of the nanotubes, which occurred during the heat treatment. In crystalline materials with many defects, the probability of electrons and holes recombination is higher. This might have made the reduction of platinum ions less probable, and hence not much platinum was deposited on the surface of topo POX materials. As discussed earlier, the band gap of the topo material is smaller than that of the non topo POX. This lack of driving force may also account for the poor platinum photodeposition.

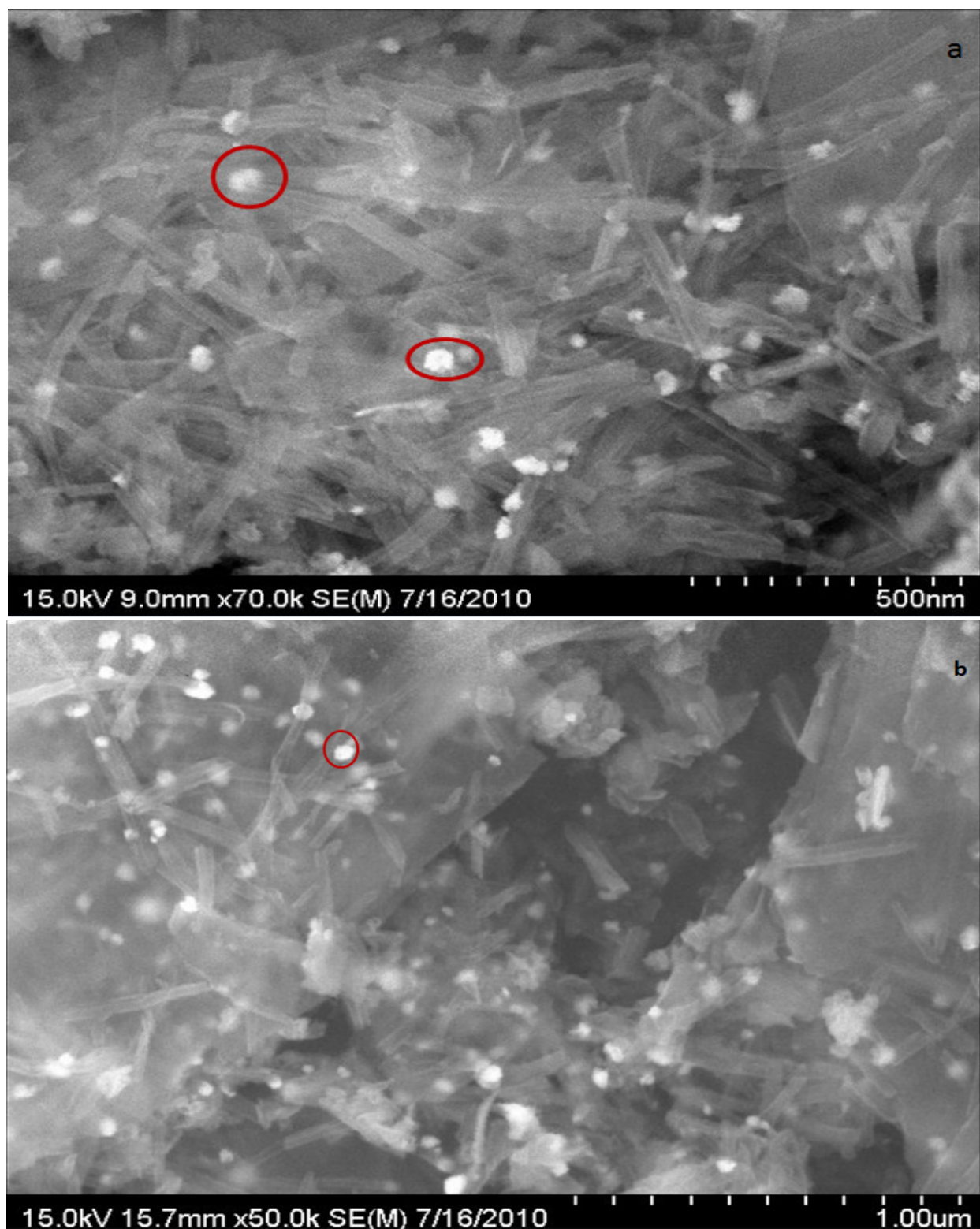


Figure 3.2(a-b): SEM images of platinum deposited on non-topo POX material.



Figure 3.3 (a-b): SEM images of platinum deposited on topo POX material.

3.1.3. TEM analysis of metal deposited POX materials

Platinum deposited POX materials were also analyzed for particle size distribution and deposition patterns using transmission electron microscopy (TEM). Non-topo POX and topo POX were diluted in DI water and a drop from each aliquot was placed on Formvar coated 200 mesh copper grids. The samples were dried in air and then analyzed in the TEM.

Figure 3.4 (a-b) shows the TEM images of platinum deposited on the surface of non-topo POX. As seen in the SEM analysis, the deposition pattern of platinum is random without any site preferences. The particle size of the platinum was also found to be between 20 and 55 nm.

Figures 3.5 (a-b) show the TEM images of platinum deposited on the surface of the topo POX material. The analysis shows that there are fewer platinum particles deposited onto the surface of the topo POX material compared to non-topo. The possible reason for this decreased deposition is discussed in section 3.1.2.

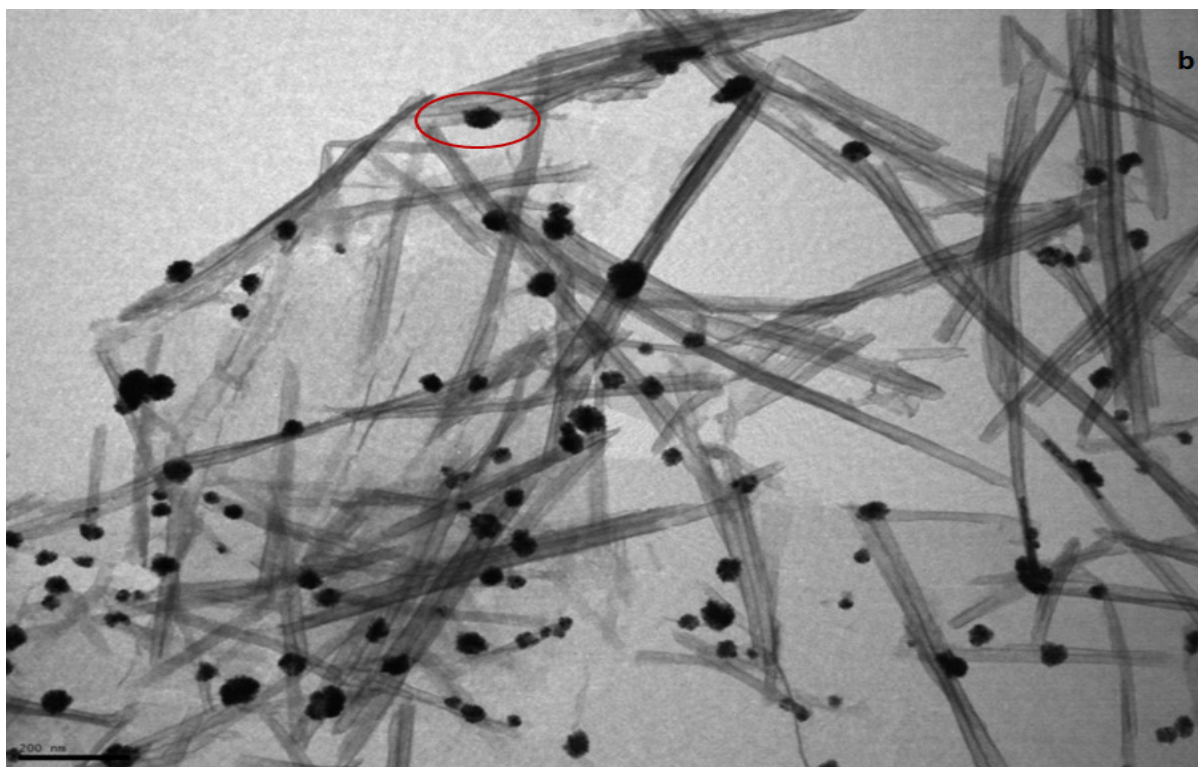
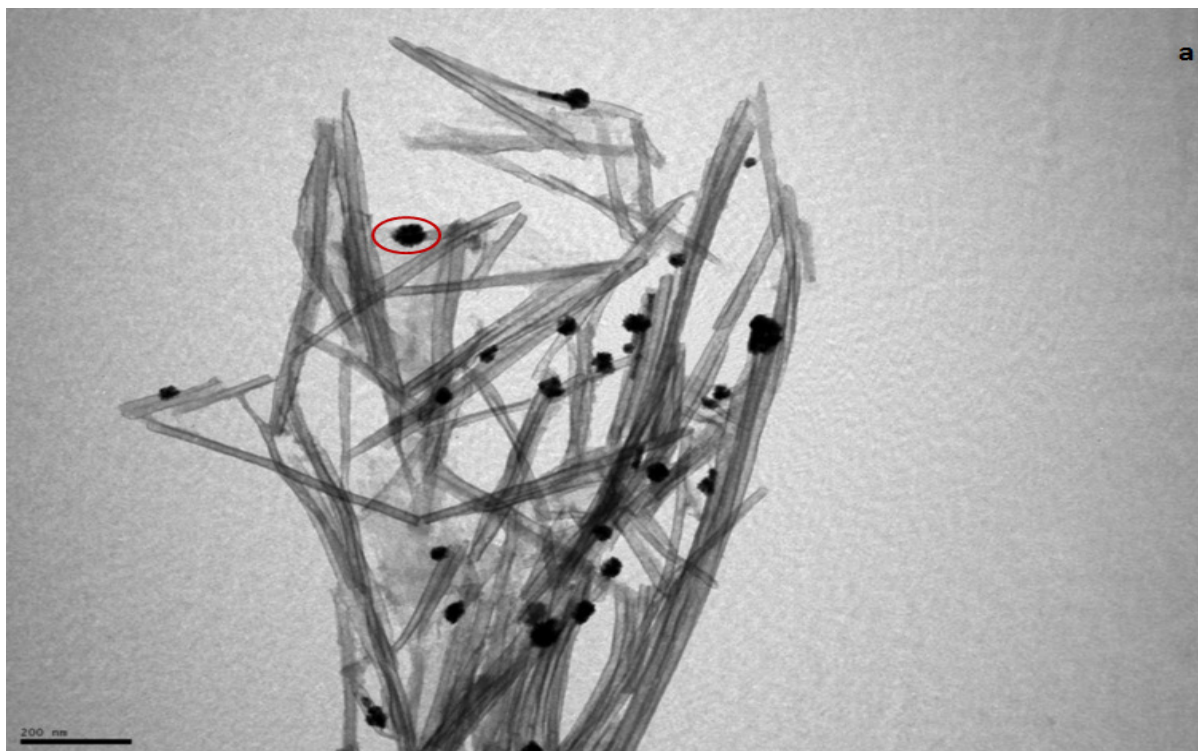


Figure 3.4 (a-b): TEM images of platinum deposited on non-topo POX material.

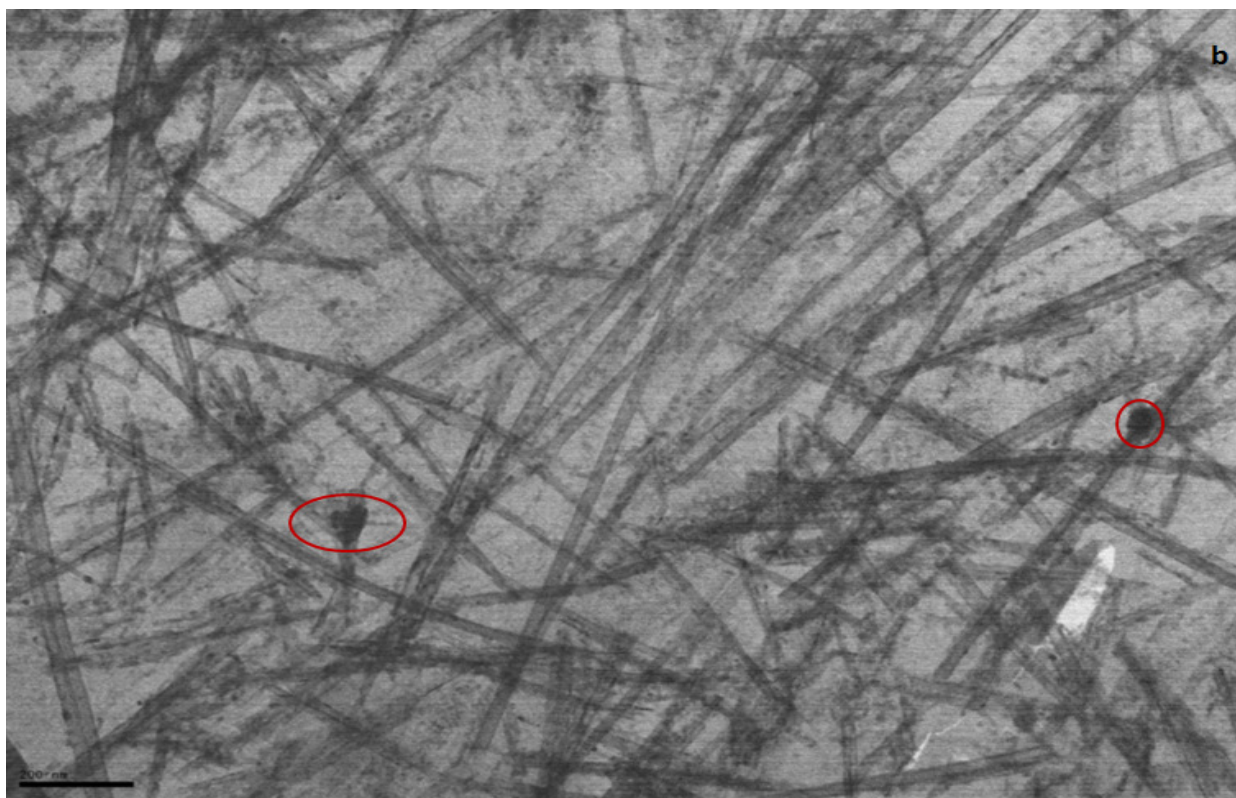
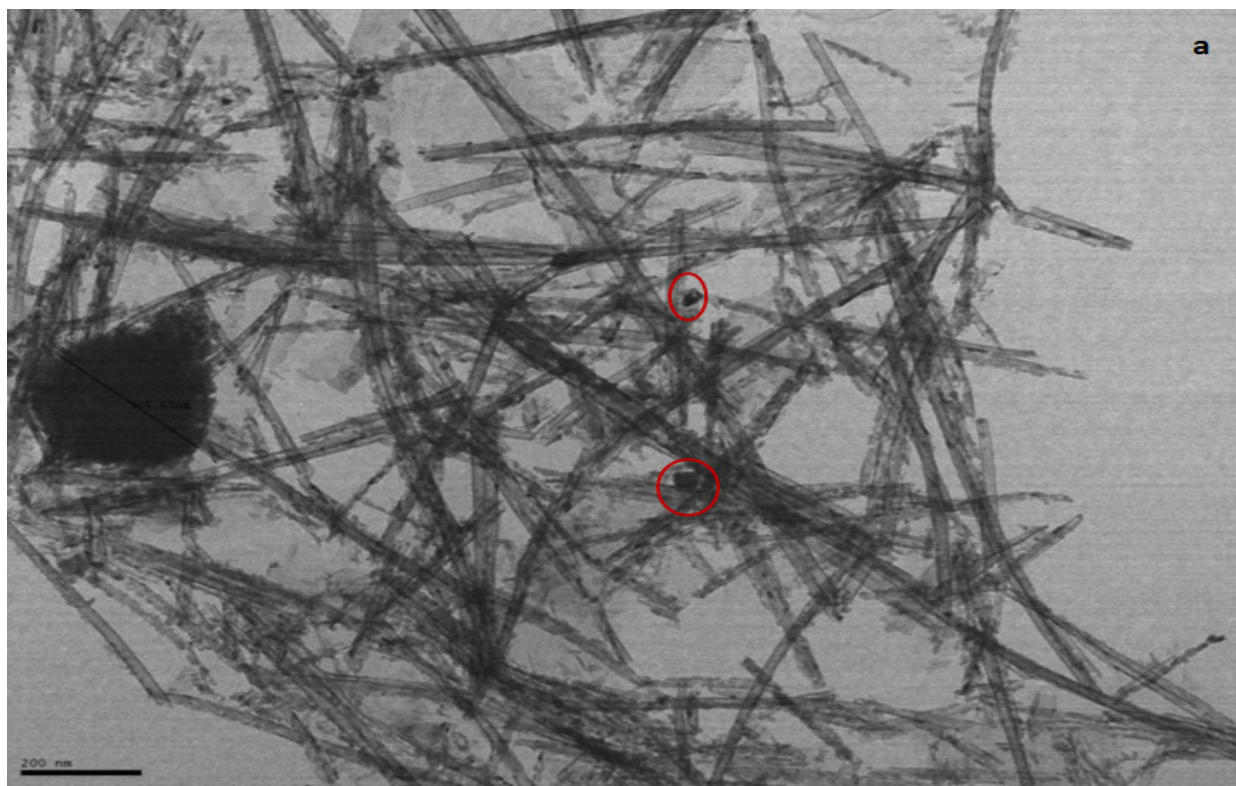


Figure 3.5 (a-b): TEM images of platinum deposited on topo POX material.

3.1.4. Inductively Coupled Plasma – Optical Emission Spectroscopy Analysis

ICP-OES analyses for the 5% platinum deposited POX (non-topo and topo) material and the supernatant (non-topo and topo) liquids were carried out. Table 3.2 shows the results for the presence of platinum in the samples. It is clearly seen that the weight % for the non topo POX solid is high, which confirms that most of platinum has been deposited on it. The topo POX has only 0.45 weight % Pt.

Table 3.2: ICP-OES analysis for the metal deposited solid POX and its supernatant.

Type of Sample	Pt (wt %)
H ₄ Nb ₆ O ₁₇ – Pt deposited non topo POX	4.6
Nb ₆ O ₁₅ – Pt deposited topo POX	0.45
H ₄ Nb ₆ O ₁₇ – Supernatant Pt non topo	0.4
Nb ₆ O ₁₅ - Supernatant Pt non topo	4.55

3.2. Calibration curve for hydrogen measurement

The amount of hydrogen evolved during the metal reduction was measured using a gas chromatograph equipped with thermal conductivity detector (TDC) and a standard reverse phase capillary column (Agilent 7890A). The temperature set up for the inlet, oven and detector were 40 °C, 20 °C and 200 °C respectively. It was calibrated using standard concentrations made by diluting pure hydrogen gas from a compressed gas cylinder. This was done by using a 1 L volumetric flask which was first sealed tightly with a rubber septum and purged with argon gas to remove air. Then, standard amounts of hydrogen gas were added. For each standard of

hydrogen gas, prepared 0.20 mL was withdrawn through the rubber septum with a gas syringe (Gas tight-1750, Hamilton Company, Nevada, USA) and injected into the gas chromatograph. Figure 3.6 shows the hydrogen calibration graph.

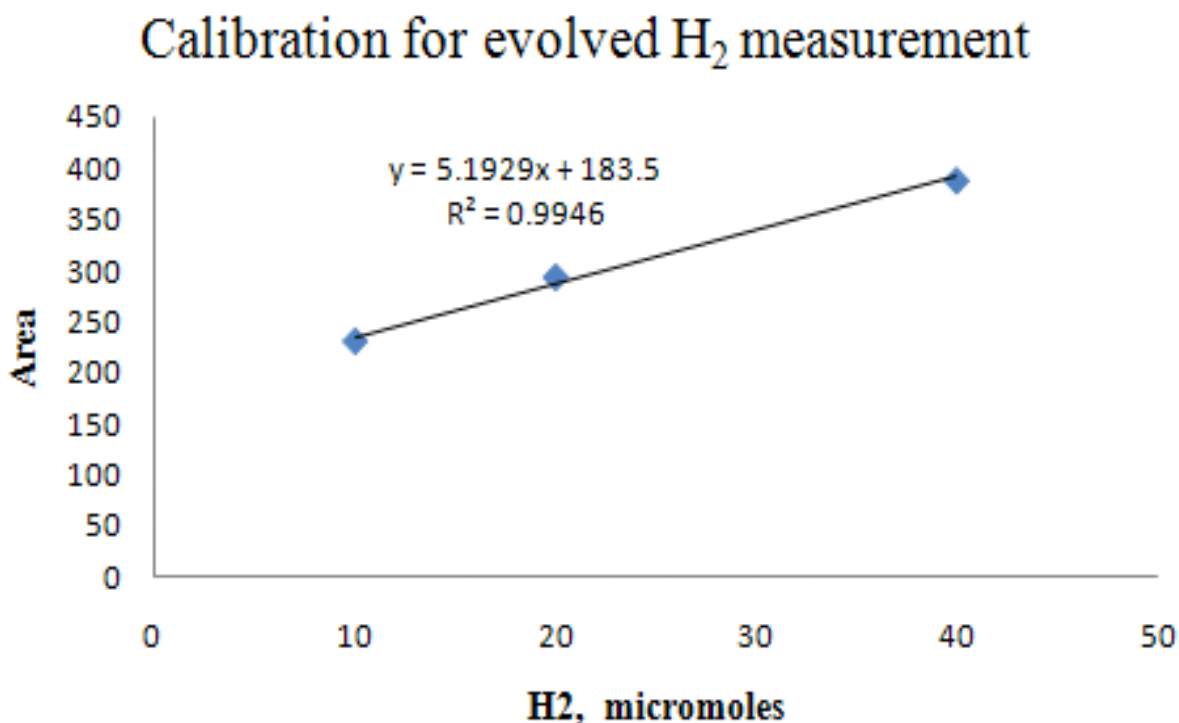


Figure 3.6: Hydrogen Calibration graph.

3.3. Hydrogen Evolution by Non-Topo and Topo POX Materials

3.3.1. Experimental set up

A fixed amount (0.015 g in all the experiments) of the POX material (non-topo and topo), and the required amount of aqueous 100 ppm platinum solution and 0.2% nitric acid (Table 3.1) were placed in a 16 cm long quartz tube. 1.0 mL of anhydrous ethanol was then added as electron donor. A magnetic Teflon stir bar was placed inside the tube and the tube was sealed

with a rubber septum. The solution and headspace gases were purged with argon gas to remove dissolved gases. The tube was placed over a stir plate in a dark room, facing a Penray Hg light bulb at a distance of 20 mm (face to face). The Hg bulb was turned on to irradiate the samples (Figure 3.7).

After every 15 minutes, 0.20 mL of the headspace gas was withdrawn with a sample lock syringe and injected into a gas chromatograph. The withdrawn gas was replaced with an equal amount of argon gas.

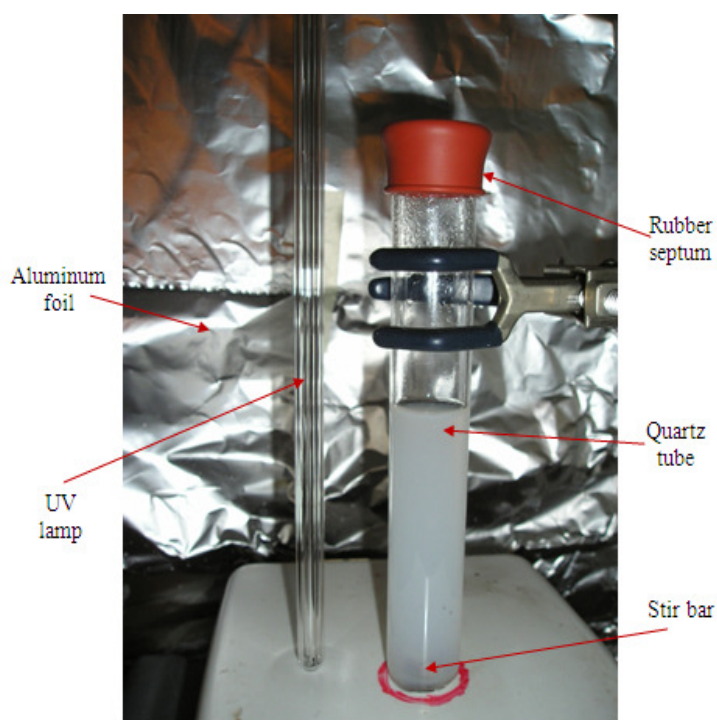


Figure 3.7: Experimental set up for hydrogen evolution under UV light.

3.3.2. Hydrogen Evolution by non topo $\text{H}_4\text{Nb}_6\text{O}_{17}$

Photocatalytic evolution of hydrogen using 0.5, 1, 2 and 5% platinum deposited on non-topo POX material is presented in Figure 3.8. The graph shows that all the metal deposited catalysts have higher activity for hydrogen production compared to non-topo POX without

platinum. The 0.5% metal deposited POX has the highest efficiency in hydrogen production within the first 45 minutes of the reaction. However, the rate of hydrogen production appears to be higher in the case of 5% Pt after 45 minutes. The error in the data is in the range of 5-10%, so these differences are not extreme.

The five different percentage metal loaded POX materials showed similar rate of photoactivity through the first 30 minutes. After 30 minutes of reaction, 0.5% and 5% metal loaded POX had significant increases in their activity, compared to the rest. It is important to remember that initially, Pt is being photoreduced by photoelectrons. So, there is an induction period that occurs for these data, before H_2 is generated. Previous studies have shown this metal deposition time to be about 30 minutes for these kinds of materials (unpublished results).

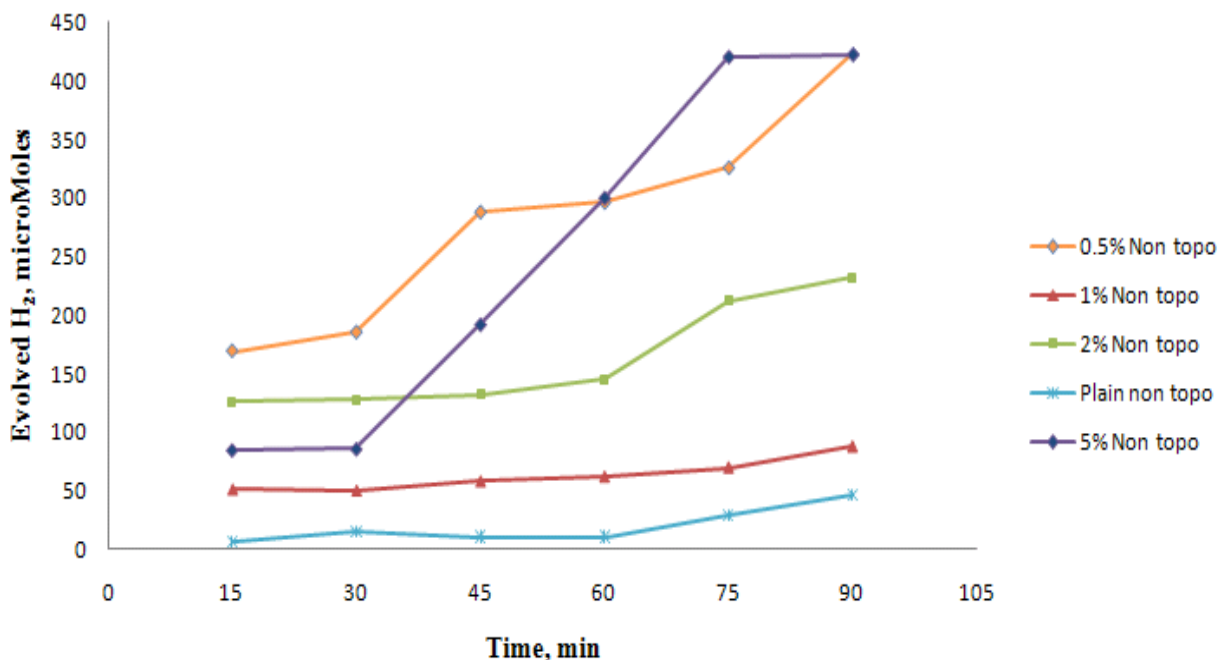


Figure 3.8: Hydrogen evolution by non topo $H_4Nb_6O_{17}$ at different loading percentage of platinum.

With the exception of 0.5% samples, the photocatalytic activity follows the order of metal percentage: 5% Pt > 2% Pt > 1% Pt. The higher activity of POX deposited with 5% metal deposited could be related to the increased number of platinum particles on the surface, in comparison with the number of platinum particles in 1 and 2% of platinum loading. As the SEM data has shown (Figure 3.9) the average particle size is similar for 1, 2 and 5 % metal deposited non-topo POX is similar (~ 50 nm). It seems to be logical that a higher percentage of metal results in higher catalytic activity because the extra metal is not producing larger particles, but more particles.



Figure 3.9: 2% platinum loaded non topo POX.

In the case of 0.5% platinum deposition, the high photocatalytic activity could correspond to the smaller metal particles, (~ 20 nm) (Figure 3.10) which maybe present not only on the

surface, but also on the internal side of the nanotubes. These well dispersed particles may correspond to the high photoactivity of this material. Other groups working in this field have also found maxima in H_2 production with Pt loadings on semiconductors near 0.5%.

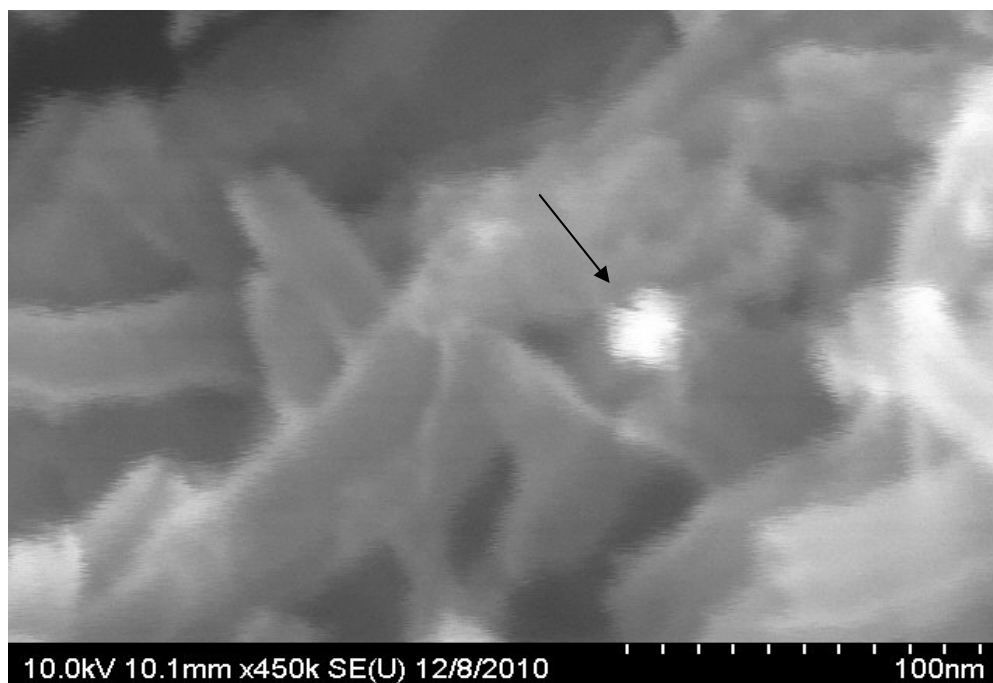


Figure 3.10: 0.5% platinum loaded non topo POX.

3.3.3. Comparison of Hydrogen Evolution of non topo POX and topo POX

The hydrogen evolution by 5% platinum loaded topo POX was carried out and compared with the 5% platinum deposited on non-topo POX (Figure 3.11). It was expected that the topotactic dehydrated POX material would show higher photoactivity due to its covalent bonding changes. But the photocatalytic activity of 5% platinum on non-topo is significantly higher than that of the 5% platinum on topo material. This could be due to the apparent decomposition of the nano-tubes producing small sections during the thermal treatment (confirmed by SEM and TEM

images). This decomposition may result in the decrease of the life time of the electrons and holes. The produced electrons and holes recombined very easily in materials with many trap sites, thereby the photoactivity of the topo POX decreases. Therefore, it is believed that the decreased photocatalytic activity of topo POX is more related to its decomposed structure rather than the metal loading.

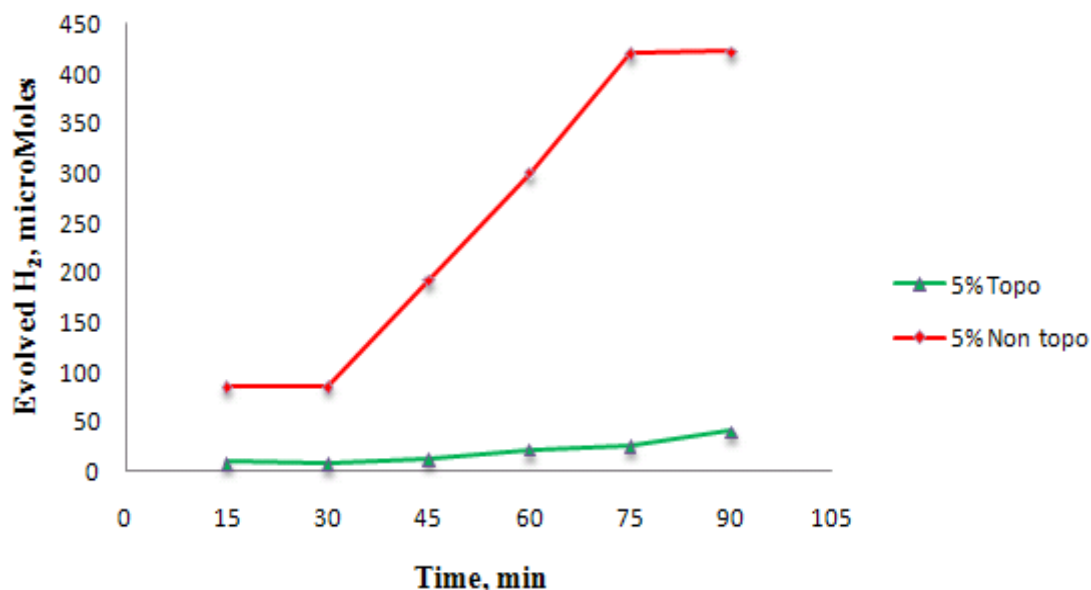


Figure 3.11: Hydrogen evolution by 5% metal loaded non topo and topo POX.

3.4. Quantum Efficiency of Hydrogen Evolution

Quantum efficiency of H₂ evolution was calculated using the following equation:

Apparent quantum yield (AQY),

$$AQY(\%) = \left(\frac{R}{I} \right) \times 100 \dots\dots\dots (1)$$

Where R and I represent the maximum rate at which H₂ molecules were evolved and the rate at which photons impinge on the sample, respectively.

$$n = \frac{p\lambda}{hc} \dots\dots\dots (2)$$

n, p, λ, h, and c are the number of photons, power of photons in watts, wavelength of UV light (254 nm), Planck's constant (6.626x10⁻³⁴ Joule/sec) and the speed of light (2.99x10¹⁷ m/sec) respectively. Number of photons involved in UV photocatalytic system was measured using a light power meter (PM 100, Thorlabs Inc., Newton, New Jersey, USA) in conjunction with a thermal sensor (S212A-10 W, Thorlabs Inc., Newton, New Jersey, USA).

The light power meter has a sensor with 1.6 cm diameter (= 2.01cm²). The UV light gave a reading of 11.98 mW on the power meter, indicating a 5.96 mW/cm² irradiance onto the quartz tube reactor. The irradiated area of the quartz tube was 8.50 cm by 2.51 cm or 21 cm². So, the sample irradiance was 125 mW or 0.125 W. The number of photons is then 1.63x10¹⁷/sec or 5.86x10²⁰/hr from equation 2. The 5% Pt deposited non topo POX materials produced 300 μmoles of hydrogen in one hour. So the apparent quantum Yield (AQY) is 63%, from equation 1. Table 3.3 shows the apparent quantum yields for different percentages metal loadings. The highest AQY was found to be for 5% metal loading non topo POX, followed by 0.5% non topo, 2% non topo, 1% non topo and the least was found for 5% topo POX.

Table 3.3: Summary of Apparent Quantum Yields for different percentages metal loading.

% Metal loaded materials	% Quantum Yields
0.5% Non topo	62
1% Non topo	4.8
2% Non topo	14.3
5% Non topo	63
5% Topo	4.6

3.5. Conclusions

This thesis research was aimed at developing high efficiency photocatalysts, which could lead to photo splitting of water to produce hydrogen as a source of renewable energy to help meet the major energy demands of the world. The synthesized nanotube POX material, $\text{H}_4\text{Nb}_6\text{O}_{17}$, has a high surface area and is a wide band gap semiconductor. In UV light, the non topo POX exhibited impressive results in terms of hydrogen evolution, whereas the topo POX showed poor photoactivity due to its decomposition. The highest AQY was found to be 63% for 5% metal loaded non topo POX, closely followed by 0.5% non topo POX at 62%. It was expected that the topotactic dehydrated POX would show better activity, but due to decomposition of the nanotubes it failed to do so. Nonetheless, the non topo POX materials developed showed high AQY and have the potential to successfully produce hydrogen under UV. In future work, these materials show promise as photocatalysts that can be used as visible light catalysts using dye-sensitized or doping techniques.

References

1. The Outlook for Energy: A view to 2030. 2009. ExxonMobil Corporation, Irving, TX.
2. Cleveland ,C., Saundry, P. 2008. Energy Transitions Past and Future, Encyclopedia of Earth.
3. Energy - "Consumption by Fuel, 1965 - 2008". 2009. Statistical Review of World Energy.
4. Doris E., McLaren J., Healey V., and Hockett S. 2009. State of the States 2009: Renewable Energy Development and the role of Policy, Technical Report, NREL. Golden, CO.
5. World Energy Consumption & Predictions, 1970-2025. Source: International Energy Outlook. 2004.
6. IPCC, 2007: Climate Change 2007: Impacts, Adaptation and Vulnerability.
7. Peter, Vitousek M. 1994. "Beyond Global Warming: Ecology and Global Change". Ecology 75:1861–1876.
8. Texas Renewable Energy Industries Association.2010.
9. Fujishima, A., Honda,K. 1972. Electrochemical Photolysis of Water at a Semiconductor Electrode, Nature, 238,37-38.
10. Mills, A., Lee,S.K. 2002. A Web based Overview of Semiconductor Photochemistry-based Current Commercial Applications, Journal of photochemistry and Photobiology.152, 233- 247.
11. Shibata, M., Kudo, A., Tanaka, A., Domen, K., Maruya, K., Onishi, T. 1987. Photocatalytic Activities of Layered Titanium Compounds and their Derivatives for H₂ Evolution from

- Aqueous Methanol Solution. Chem. Lett., 6, 1017-1018.
12. Takata, T., Furumi, Y., Shinohara, K., Tanaka, A., Hara, M., Kondo, J. N., Domen, K. 1997.
Photocatalytic Decomposition of Water on Spontaneously Hydrated Layered Perovskites.
Chem. Mater. 9 (5), 1063-1068.
13. Takata, T., Furumi, Y., Shinohara, K., Tanaka, A., Hara, M., Kondo, J. N., Domen, K. 1997.
A Highly Active Photocatalyst for Overall Water Splitting with a Hydrated Layered
Perovskite Structure. J. Photochem. Photobiol. A: Chemistry., 106, 45-49.
14. Ikeda, S., Hara, M., Kondo, J.N., Domen, K., Takahashi, H., Okubo, T., Kakihana, M. 1998.
Preparation of A High Active Photocatalyst, $K_2La_2Ti_3O_{10}$, by Polymerized Complex Method
and Its Photocatalytic Activity of Water Splitting. J. Mater. Res.13 (4), 852-855.
15. Domen, K., Ebina, Y., Sekine, T., Tanaka, A., Kondo, J., Hirose, C. 1993. Ion-Exchangeable
Layered Niobates as Photocatalysts. Catalysis Today.16, 479-486.
16. Domen, K., Yoshimura, J., Sekine, T., Tanaka, A., Onishi, T. 1990. A Novel Series of
Photocatalysts with an Ion-Exchangeable Layered Structure of Niobate. Catalysis Letters.
4, 339-344.
17. Kim, Y. I., Salim, S., Huq, M. J., Mallouk, T. E. 1991. Visible Light Photolysis of Hydrogen
Iodide Using Sensitized Layered Semiconductor Particles. Journal of American Chemical
Society.113 (25), 9561-9563.
18. Kim, Y. I., Atherton, S. J., Brigham, E. S., Mallouk, T. E. 1993. Sensitized Layered Metal
Oxide Semiconductor Particles for Photochemical Hydrogen Evolution Donors. Journal of

Physical chemistry. 97, 11802-11810.

19. Kresge, C. T., Leonowicz, M. E., Roth, W. J., Vartuli, J. C., Beck, J. S. 1992. Ordered Mesoporous Molecular Sieves Synthesized by a Liquid-Crystal Template Mechanism. *Nature*. 359, 710-712.
20. Beck, J. S., Vartuli, J. C. Roth, W. J., Leonowicz, M. E., Kresge, C. T.; Schmitt, K. D., Chu, C. T. W., Olson, D. H., Sheppard, E. W., McCullen, S. B., Higgins, J. B., Schlemker, J. L. 1992. A New Family of Mesoporous Molecular-Sieves Prepared with Liquid-Crystal Templates. *Journal of American Chemical Society*. 114, 10834-10843.
21. Kresge, C. T., Leonowicz, M. E., Roth, W. J., Vartuli, J. C. 1992. Synthetic Porous Crystalline Material. Mobil Oil Corp. US Patent 5098684.
22. Carreon, M. A., Gulians, V. V. 2005. Ordered Meso and Macroporous Binary and Mixed Metal Oxides (A Review). *European Journal of Inorganic Chemistry*. 1, 27-43.
23. Sayama, K., Tanaka, A., Domen, ., Maruya, K., Onishi, T. 1991 Photocatalytic Decomposition of Water Over Platinum- Intercalated $K_4Nb_6O_{17}$. *Journal of Physical Chemistry*. 95 (3), 1345-1348.
24. Samuneva, B., Dimitrov, K. St. V. 1991. Structure and Optical Properties of Niobium Silicate Glasses. *Journal of Non-Crystal Solids*. 129, 54-63.
25. Domen, K., Kudo, A., Shinozaki, A., Tanaka, A., Maruyama, K., Onishi, T. 1986. Photodecomposition of Water and Hydrogen Evolution from Aqueous Methanol Solution over Novel Niobate Photocatalysts. *Journal of the Chemical Society, Chemical*.

Communications.95 (4), 356-357.

26. Kim, Y. I., Keller, S. W., Krueger, J. S., Yonemoto, E. H., Saupe, G. B., Mallouk, T. E.1997.

Photochemical Charge-Transfer and hydrogen Evolution Mediated by Oxide

Semiconductor Particles in Zeolite-Based Molecular Assemblies. Journal of Physical

Chemistry B.101 (14), 2491-2500.

27. Yesu, N. R. 2006. New Porous Oxides from Layered Semiconductors. M.Sc. Thesis,

University of Texas at El Paso.

28. Bizeto,M.A., Constatino,V.R.L. 2004. Structural Aspects and Thermal Behavior of the

Proton Exchanged Layered Niobate $K_4Nb_6O_{17}$. Material Research Bulletin 39, 1729-1736.

29. Anpo M., Takeuchi M. 2003. The Design and Development of Highly Reactive Titanium

Oxide Photocatalysts Operating under Visible Light Irradiation, Journal of Catalysis 216,

505-516.

30. Kitano, M., Tsujimaru, K., Anpo, M. 2006. Decomposition of Water in the Separate

Evolution of Hydrogen and Oxygen using Visible Light-Responsive TiO_2 Thin Film

Photocatalysts: Effect of the Work Function of the Substrates on the Yield of the Reaction.

Applied Catalysis A: General, 314,179-183.

31. Takabayashi S., Nakamura R., Nakato Y. 2004. A Nano-Modified Si/TiO_2 Composite

Electrode for Efficient Solar Water Splitting, Journal of Photochemistry and Photobiology.

A: Chemistry. 166(1-3), 107-113.

32. Thimsen E., Rastgar N., Biswas P. 2008. Nanostructured TiO_2 Films with Controlled

Morphology Synthesized in a Single Step Process: Performance of Dye-Sensitized Solar

Cells and Photo Water splitting. Journal of Physical Chemistry. 112(11), 4134-4140.

33. Jang J.S., Kim H.G., Reddy V.R, Bae S.W., Ji S.M., Lee J.S. 2005. Photocatalytic Water Splitting over Iron Oxide Nanoparticles Intercalated in HTiNb(Ta)O₅ Layered Compounds, Journal of Catalysis. 231, 213-222.
34. Bizeto, M.A., Shiguihara, A.L., Constatino, V.R.L. 2009. Layered Niobate Nanosheets: Building blocks for Advanced Material Assembly. Journal of Materials Chemistry 19, 2512-2525.
35. Du G., Chen Q., Yu Y., Zhang S., Zhou W., Peng L. M. 2004. Synthesis, Modification and Characterization of K₄Nb₆O₁₇-type Nanotubes. J. Mater. Chemistry. **14**, 1437.
36. Next big future. 2009. 22 November 2010 <<http://nextbigfuture.com/2009/06/supercritical-co2-recompression-cycle.html>>
37. Wikipedia. 2008. 8/19/2008. 22 November 2010.
<http://commons.wikimedia.org/wiki/File:Simens_numeri.jpg>
38. Creative Commons Attribution-Share Alike 3.0 Unported. 2010. 22 November 2010.
< [http://en.wikipedia.org/wiki/File:Schema_MEB_\(en\).svg](http://en.wikipedia.org/wiki/File:Schema_MEB_(en).svg)>
39. Oxford Instruments, UK. 2009. 22 November 2010.
< <http://www.oxford-instruments.com/applications-markets/environment/environmental-monitoring/rohs/Pages/x-ray-fluorescence-xrf.aspx>>
40. Particle and surface sciences Pty. Limited. 2008. 22 November 2010.
< http://www.pss.aus.net/products/micromeritics/equip_surface_area/2010/2020.html>
41. New Mexico State University. 2008. 22 November 2010.
< www.chemistry.nmsu.edu/Instrumentation/NMSU_Optima2100.html>
42. Chemguide. 2006. 24 November 2010.
<<http://www.chemguide.co.uk/analysis/uvvisible/spectrometer.html>>

Curriculum Vita

Saroja Pradhan was born in Samtse, Bhutan on February 29, 1980 to Mr. Amber Kumar Pradhan and Subhadra Devi Pradhan. She received her Bachelor of Science degree with a major in Biology and minor in Chemistry from Sherubtse College, Bhutan in December 2003. She did her Postgraduate Certificate in Education (PGCE) in 2005 and started teaching at Kanglung High School in January, 2006. She taught Biology and Chemistry for two and a half years. She received a Bhutanese Cultural Endowed Scholarship from the University of Texas at El Paso to pursue her Master studies. She joined UTEP in the fall semester of 2008 as a master student in the Department of Chemistry. She worked under the guidance of Dr. Geoffrey B. Saupe, Associate Professor, Department of Chemistry, UTEP. Her thesis was entitled DEVELOPMENT OF NANOTUBE HEXANIOBATE FOR PHOTOCATALYTIC PRODUCTION OF HYDROGEN FROM WATER.

Permanent Address:

Bahunitar,

Chargharey, Samtse.

Bhutan.

This thesis was typed by Saroja Pradhan